Clues to the lithospheric structure of Mars from wrinkle ridge sets and localization instability

Laurent G. J. Montési[1] and Maria T. Zuber[2]
Massachusetts Institute of Technology, Cambridge, Massachusetts, USA

Received 3 September 2002; revised 5 February 2003; accepted 12 March 2003; published 5 June 2003.

[1] Wrinkle ridges are a manifestation of horizontal shortening in planetary lithospheres, for which deformation is localized on faults that underlie individual ridges. In ridged plains of Mars, such as Solis Planum or Lunae Planum, wrinkle ridges are spaced ~40 km apart, whereas in the Martian northern lowlands, where ridges are identified only in Mars Observed Laser Altimeter (MOLA) altimetric data, the ridge spacing is at least ~80 km. We attribute ridge spacing to an instability of the lithosphere under horizontal compression. The localization instability, which results in periodically spaced faults [*Montési and Zuber*, 2003a], links the difference of ridge spacing in the northern lowlands and in the highland ridged plains to the difference of crustal thickness via the depth of the brittle-ductile transition (BDT). In Solis and Lunae Plana, where the crust is 50 to 60 km thick, the crust may be ductile at depth, limiting faulting to the BDT of crustal rocks. In the lowlands, the crust is only about 30 km thick and may be brittle throughout. Thus the depth of faulting may be controlled by the BDT of mantle rocks, which is roughly a factor of two deeper than that of crustal rocks. The geotherm can be identical in both regions, at 12 ± 3 K.km^{-1}, although differences of a few K.km^{-1} can be accommodated within this model. The heat flux implied by this geotherm is similar to the heat produced by radiogenic decay 3 Gyr ago. Our analysis provides a rheological explanation for the difference in spacing between ridges in the highlands and the lowlands, in contrast to the suggestion of *Head et al.* [2002], who proposed that alternating lowlands ridges are buried by sediments. In addition, finite element models that use the lithospheric structure deduced from ridge spacing show that modest gradients of crustal thickness or heat flux across a ridged plains favor the formation of faults dipping toward high-elevation areas, as may be the case in Solis Planum [*Golombek et al.*, 2001]. *INDEX TERMS:* 5475 Planetology: Solid Surface Planets: Tectonics (8149); 5455 Planetology: Solid Surface Planets: Origin and evolution; 5418 Planetology: Solid Surface Planets: Heat flow; 8120 Tectonophysics: Dynamics of lithosphere and mantle—general; 3210 Mathematical Geophysics: Modeling; *KEYWORDS:* wrinkle ridges, faulting, Mars, heat flow, strength envelope

Citation: Montési, L. G. J., and M. T. Zuber, Clues to the lithospheric structure of Mars from wrinkle ridge sets and localization instability, *J. Geophys. Res.*, *108*(E6), 5048, doi:10.1029/2002JE001974, 2003.

1. Introduction

[2] The structure and evolution of planetary lithospheres helps to constrain the thermal history of a planet. As no direct subsurface information is available for objects other than the Earth and Moon, the three-dimensional structure of the lithosphere of other planets must be inferred from modeling of remote sensing data such as multispectral and panchromatic images, surface topography, and the gravity and magnetic fields. In particular, the vertical strength profile of planetary lithospheres can be constrained from the horizontal length scale of tectonic features. The wavelength of the flexural response to surface or subsurface loads indicates the thickness of an equivalent elastic plate [*Turcotte and Schubert*, 1982; *Comer et al.*, 1985; *Banerdt et al.*, 1992; *Wieczorek and Phillips*, 1998]; fold wavelengths are proportional to the thickness of a strong layer sometimes associated with the brittle layers of the lithosphere [*Fletcher and Hallet*, 1983; *Ricard and Froidevaux*, 1986; *Zuber*, 1987; *Zuber and Aist*, 1990]. The spacing of wrinkle ridges has been used to infer the thickness of a mechanically strong layer at the top of the Martian lithosphere [*Saunders et al.*, 1981; *Zuber and Aist*, 1990; *Watters*, 1991], as will be done here. Depending on the model used, however, wrinkle ridge spacing can imply deep penetration of ridge-related deformation (several to tens of kilometers), most consistent with the influence of global stress patterns on ridge orientation [*Zuber and Aist*, 1990; *Banerdt et al.*, 1992; *Zuber*, 1995], or the presence of a

[1]Now at Woods Hole Oceanographic Institution, Woods Hole, Massachusetts, USA.
[2]Also at Laboratory for Terrestrial Physics, NASA Goddard Space Flight Center, Greenbelt, Maryland, USA.

0148-0227/03/2002JE001974$09.00

shallow weak layer (1 to 2 km deep) related to a possible megaregolith at the base of volcanic plains [*Saunders et al.*, 1981; *Watters*, 1991].

[3] As faulting is an important aspect of wrinkle ridge formation [*Lucchita and Klockenbrink*, 1981; *Plescia and Golombek*, 1986; *Watters*, 1988; *Allemand and Thomas*, 1992], faults have been defined a priori in previous theories of ridge formation [*Zuber*, 1995; *Schultz*, 2000]. However, fault formation, i.e., the localization of failure onto discrete shear zones, has not been included as a dynamic process. In order to relate ridge spacing and the mechanical structure of the lithosphere, the faulted layer has sometimes been regarded as pseudo-plastic [*Zuber and Aist*, 1990]. This rheology includes a yield strength at which faulting occurs, but also implies that deformation remains distributed instead of localizing on discrete shear zones. In this study, we show how the estimated thickness of the layer involved in faulting at Martian wrinkle ridges is modified by the consideration of localization, using the concept of a localization instability introduced in *Montési and Zuber* [2003a]. That the localization instability is the most likely control on fault spacing is best seen when the ridge spacing of different regions is compared. In areas where wrinkle ridges were recognized in Viking images, ridge spacing is ~40 km [*Saunders et al.*, 1981; *Zuber and Aist*, 1990; *Watters*, 1991], whereas in the northern lowlands (Figure 1a), where ridges were only recently recognized from Mars Observed Laser Altimeter (MOLA) data [*Withers and Neumann*, 2001; *Head et al.*, 2002], their spacing is ~80 km [*Head et al.*, 2002]. The localization instability can link the difference of ridge spacing to crustal thickness variations (Figure 1b).

[4] Variations of the thickness of the Martian crust have been inferred from the gravity field and topography of Mars, with the assumptions of an average crustal thickness of 50 km, density of the crust and the mantle of 2900 and 3500 kg.m^{-3}, respectively [*Zuber et al.*, 2000; *Zuber*, 2001] (Figure 1b). The precision of the gravity field implies that crustal thickness variations up to degree 40 can be confidently used for geological interpretation [*Smith and Zuber*, 2002], although additional uncertainties arise from model assumptions such as a uniform crustal density. The crust is approximately 30 km thick in the northern lowlands, and about 60 km thick in the southern highlands, with locally much reduced thickness inside impact basins (Figure 1b). These numbers depend on the assumed average crustal thickness, but the 50-km value is well constrained: smaller values would result in negative crustal thickness, whereas an overall thicker crust would relax too quickly to preserve the observed long-wavelength variations such as the degree-1 pole-to-pole crustal thickness variation and the Hellas Basin [*Zuber et al.*, 2000; *Nimmo and Stevenson*, 2001]. Although some chemical data point to either thinner (20–30 km [*Norman*, 1999]) or thicker (75–95 km [*Norman*, 2002]; 100–200 km [*Sohl and Spohn*, 1997]) crust, gravity-topography ratios constrain the average crustal thickness of Mars to be 60 ± 24 km [*Wieczorek and Zuber*, 2002] and localized gravity/topography admittances in some regions [*McGovern et al.*, 2002; *Nimmo*, 2002] are best explained by flexural models with a reference crustal thickness ~50 km, in agreement with *Zuber et al.* [2000].

[5] The difference of topography and gravity between the northern lowlands and the southern highlands might also be explained by a crust of uniform thickness that would be ~700 kg.m^{-3} denser in the North. However, at present, there is no geochemical justification for that assumption (see section 4.2) and we follow the interpretation that the Martian crust is thinner in the north than in the south.

[6] Although the Martian northern plains are technically ridged plains since ridges have been identified in the lowlands with MOLA data, we restrict herein the appellation "ridged plains" to those plains where ridges were recognized in Viking images. We present in the next section topographic models of plains with wrinkle ridges derived from MOLA data [*Smith et al.*, 2001], showing in particular the newly identified wrinkle ridges in the northern lowlands [*Withers and Neumann*, 2001; *Head et al.*, 2002] and evidence for consistent fault vergence at regional scale [*Golombek et al.*, 2001] derived from the asymmetry of individual ridges. Then, the localization instability analysis developed by *Montési and Zuber* [2003a] is applied to wrinkle ridge sets. In our preferred model, the faults underlying Martian ridges penetrate to the brittle-ductile transition (BDT), which is 30 or 60 km deep, depending on the crustal thickness and the geotherm. Finally, we present finite element models that address the origin of the vergence selectivity observed in Solis Planum [*Golombek et al.*, 2001] by appealing to lateral variations of geotherm or crustal thickness perpendicular to the ridge trend. Variations of crustal thickness within individual plains are beyond the resolution of current crustal thickness models, but there is no doubt that the crustal thickness and the heat flow under Tharsis were higher than in neighboring regions, providing a justification for the gradients used in this study. The implications of our study for the sedimentation history in the lowlands and for the thermal evolution of Mars are subsequently discussed.

2. Wrinkle Ridge Sets

2.1. Morphology of Wrinkle Ridge

[7] Wrinkle ridges are elongated and sinuous topographic highs identified at the surface of all the terrestrial planets and satellites [*Watters*, 1988, 1992] (Figure 2). They result from horizontal shortening [*Lucchita and Klockenbrink*, 1981; *Plescia and Golombek*, 1986; *Golombek et al.*, 1991]. Individual wrinkle ridges on Mars are composed of a broad swell, or ridge (up to 10 km wide, 10 to 300m high, and hundreds of kilometers long) with a summit crenulation, or wrinkle (~2 km wide, 100 m high) [*Watters*, 1988, 1993; *Schultz*, 2000; *Golombek et al.*, 2001].

[8] The ridges have an asymmetric profile that indicates that faulting was important in their formation [*Golombek et al.*, 1991; *Plescia*, 1991; *Golombek et al.*, 2001], although the relative roles of folding and faulting in forming the ridge have been much debated [*Plescia and Golombek*, 1986; *Golombek et al.*, 1991; *Watters and Robinson*, 1997]. Recent numerical models showed that the ridge morphology is consistent with folding of a near-surface layered sequence forced by a deeper blind thrust [*Niño et al.*, 1998; *Schultz*, 2000] (Figure 2). Layering in Martian examples may come from the volcanic sequence of the ridged plains. Alternatively, the backthrust may be generated at an ice-rich décollement layer [*Mangold et al.*, 1998]. In the models of *Niño et al.* [1998] and *Schultz* [2000], the wrinkles

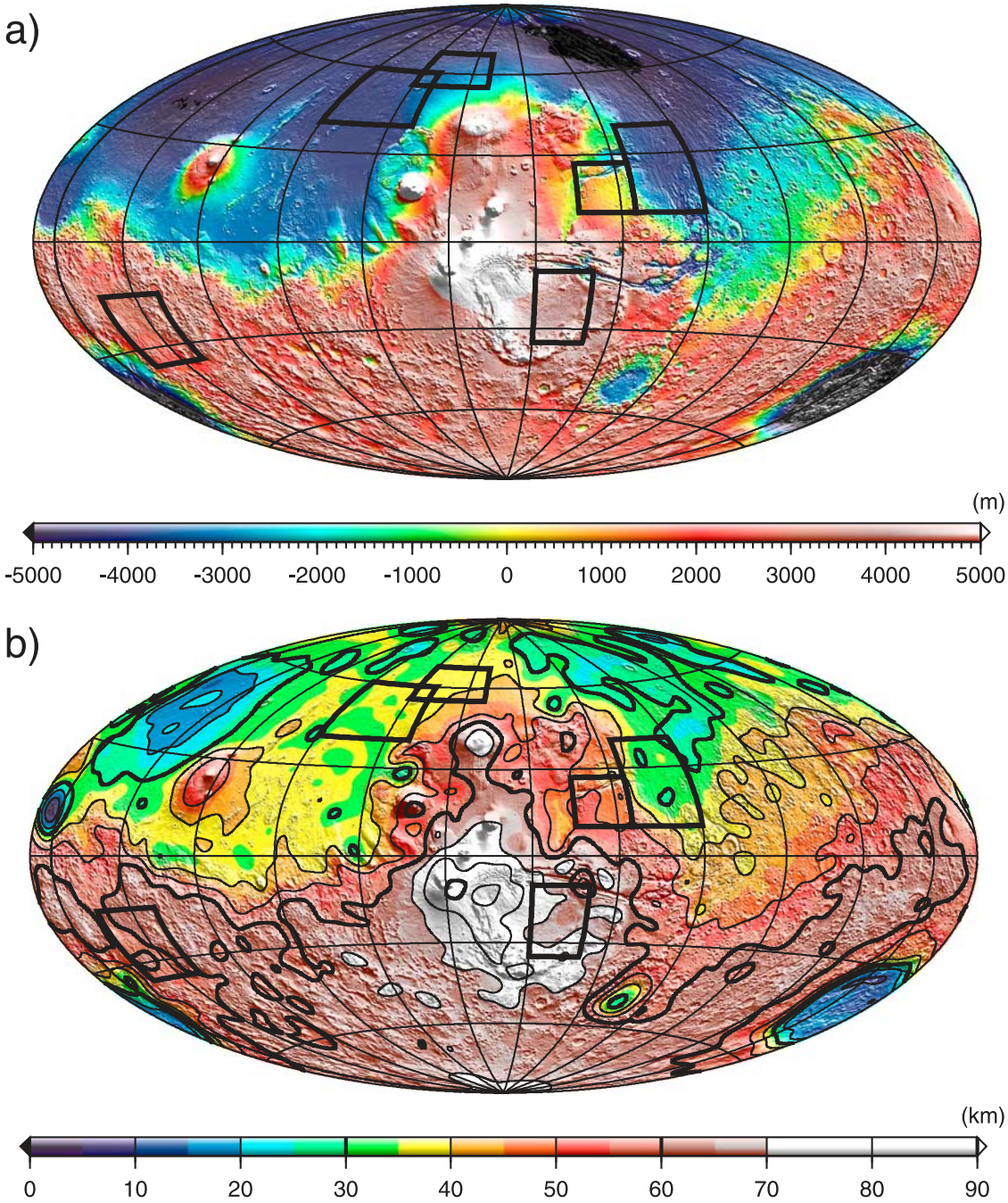

Figure 1. a) Topography from Mars Orbiter Laser Altimeter (MOLA) [from *Smith et al.*, 2001] and b) crustal thickness up to degree 40 derived from MGS data overlain on a shaded relief image of MOLA topography [from *Zuber*, 2001; *Smith and Zuber*, 2002]. Contours in b) every 10 km, thicker contours every 30 km. The boxes mark the location of the areas detailed in Figures 3 and 5. Hammer projection centered on 260°E longitude.

appear as no more than a secondary structure related either to fault propagation or to a back thrust generated by interbed slip. The origin of the wrinkle may vary along the strike of the ridge, which is consistent with observations of wrinkle switching from one side of a ridge to another or broken en échelon [*Schultz*, 2000] (Figure 2).

[9] Ridges form subparallel sets [*Maxwell*, 1982; *Watters and Maxwell*, 1986] (Figure 2) with consistent interridge spacing at regional scale [*Saunders et al.*, 1981; *Watters*, 1991]. At large scale, their pattern is concentric to global centers of tectonic and volcanic activity such as the Tharsis province on Mars [*Banerdt et al.*, 1982, 1992; *Maxwell*, 1982; *Chicarro et al.*, 1985; *Watters and Maxwell*, 1986] and Aphrodite Terra or Lada Terra on Venus [*Banerdt et al.*, 1997; *Bilotti and Suppe*, 1999]. Local centers are also recognized on Venus [*Tracadas and Zuber*, 1998; *Bilotti and Suppe*, 1999]. A Tharsis-centric pattern on Mars has been recently established by the recognition of numerous

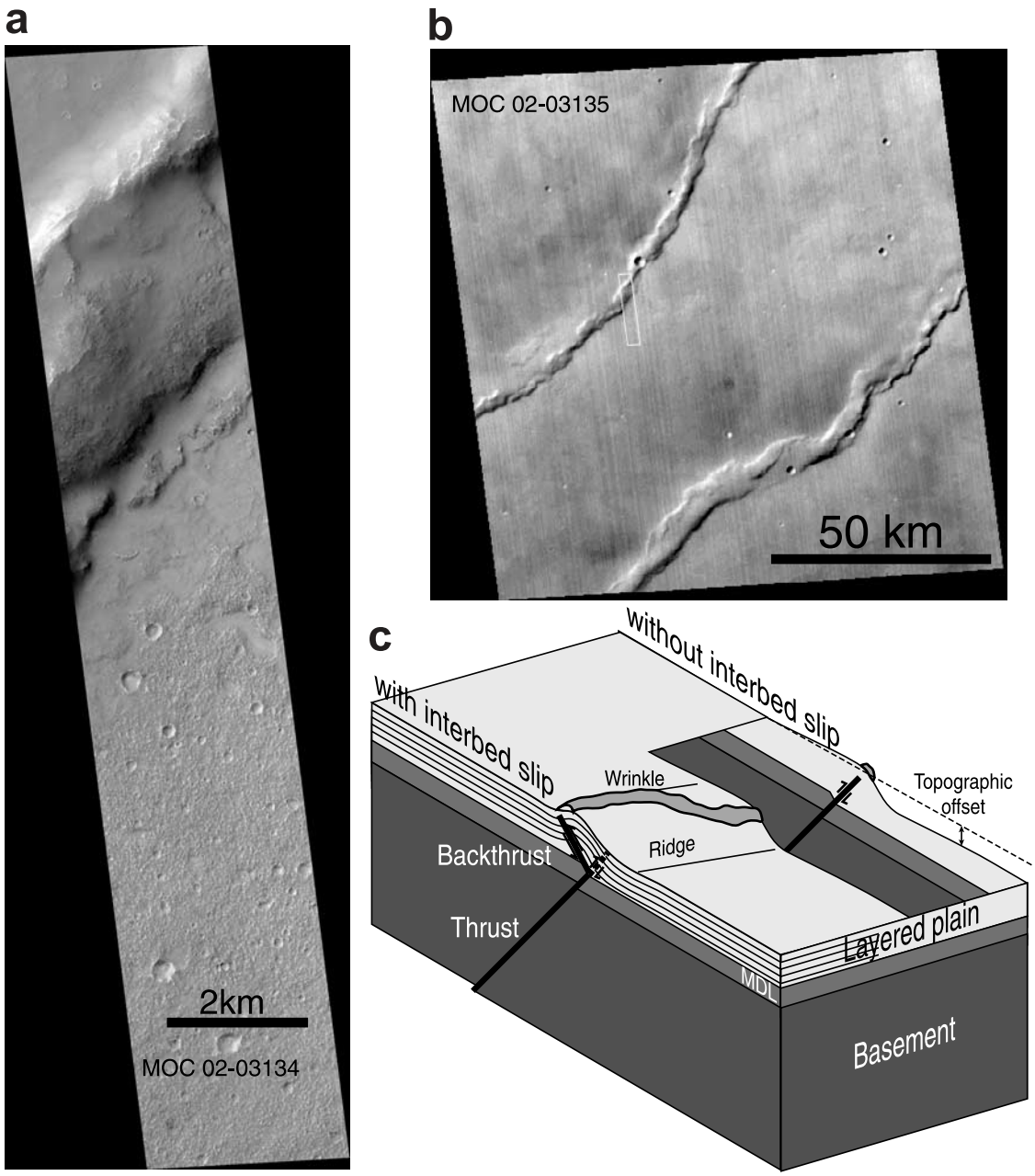

Figure 2. Mars Orbiter Camera (MOC) a) narrow angle and b) wide angle images of a wrinkle ridge in Solis Planum (NASA/JPL/Malin Space Science Systems). c) Possible subsurface structure of a wrinkle ridge [after *Schultz*, 2000; *Niño et al.*, 1998]. A blind thrust fault offsets vertically the basement underneath a layered plain unit of volcanic or sedimentary origin. A backthrust may be generated if interbed slip occurs in the layered unit. The crenulation, or wrinkle, on top of the ridge represents the shallower geometry of faults within the layered plains. MDL: Main Décollement Level, possibly ice-rich [*Mangold et al.*, 1998].

ridges in the northern lowlands using MOLA data [*Withers and Neumann*, 2001; *Thomson and Head*, 2001; *Head et al.*, 2002].

2.2. Regional Topography

[10] Two of the most intensely studied ridged plain regions on Mars are Solis Planum and Lunae Planum (Figures 3a and 3b). Both display subparallel ridge sets visible in Viking images [*Watters and Maxwell*, 1986]. They trend respectively N20°E and N–S. The ridge spacing is 40 to 50 km on average [*Saunders et al.*, 1981; *Watters*, 1991; *Head et al.*, 2002].

[11] At regional scale, both Solis Planum and Lunae Planum are tilted down to the east. Using MOLA data, *Golombek et al.* [2001] showed that the plains have a staircase-like profile, being vertically offset across individual ridges and subhorizontal to back-tilted between ridges (Figure 4). This geometry indicates that the faults under-

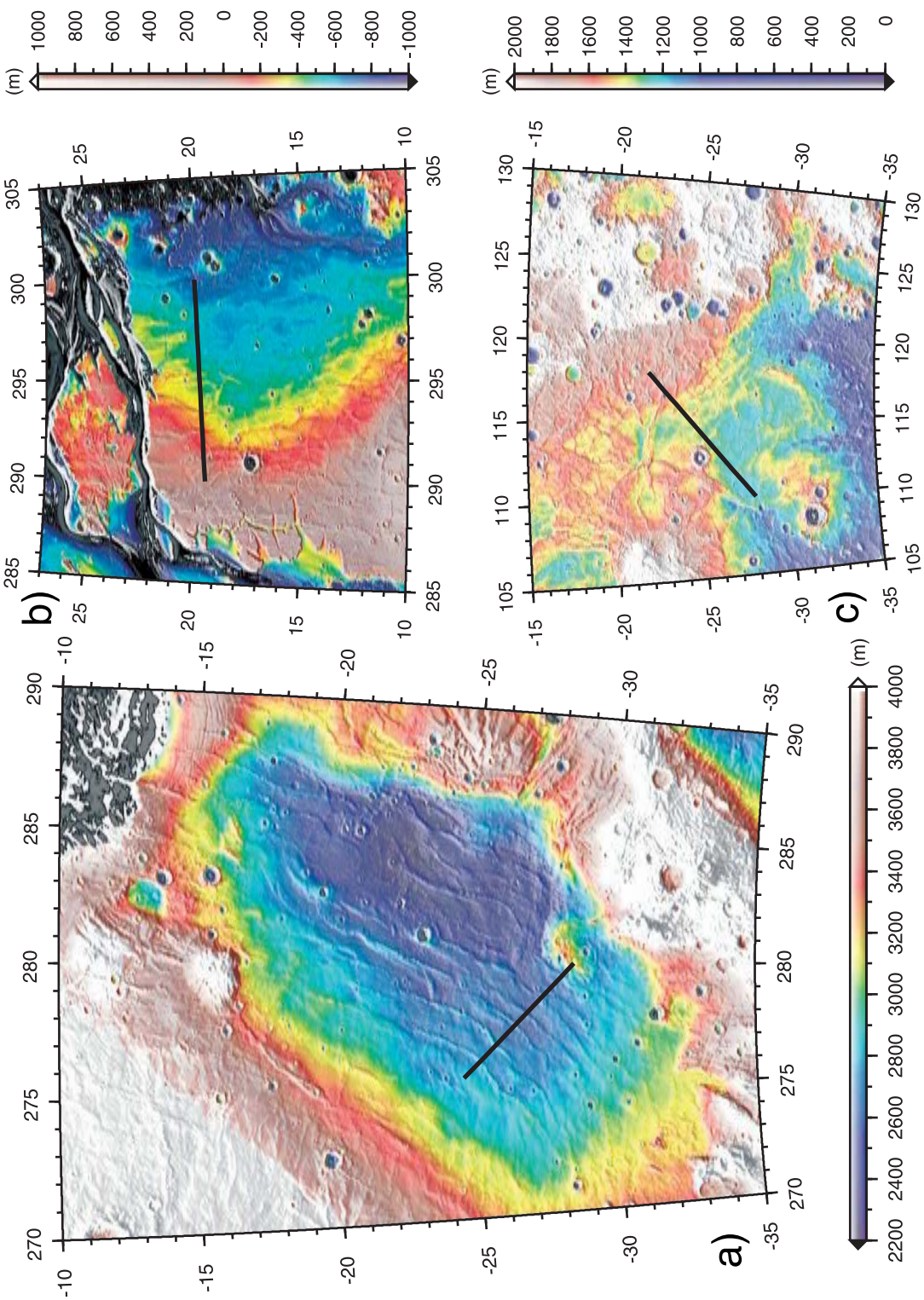

Figure 3. Digital Elevation Models of a) Solis Planum, b) northern Lunae Planum, and c) Hesperia Planum. Terrain models from Mars Orbiter Laser Altimeter (MOLA) data gridded in $2' \times 1'$ blocks [*Smith et al.*, 2001].

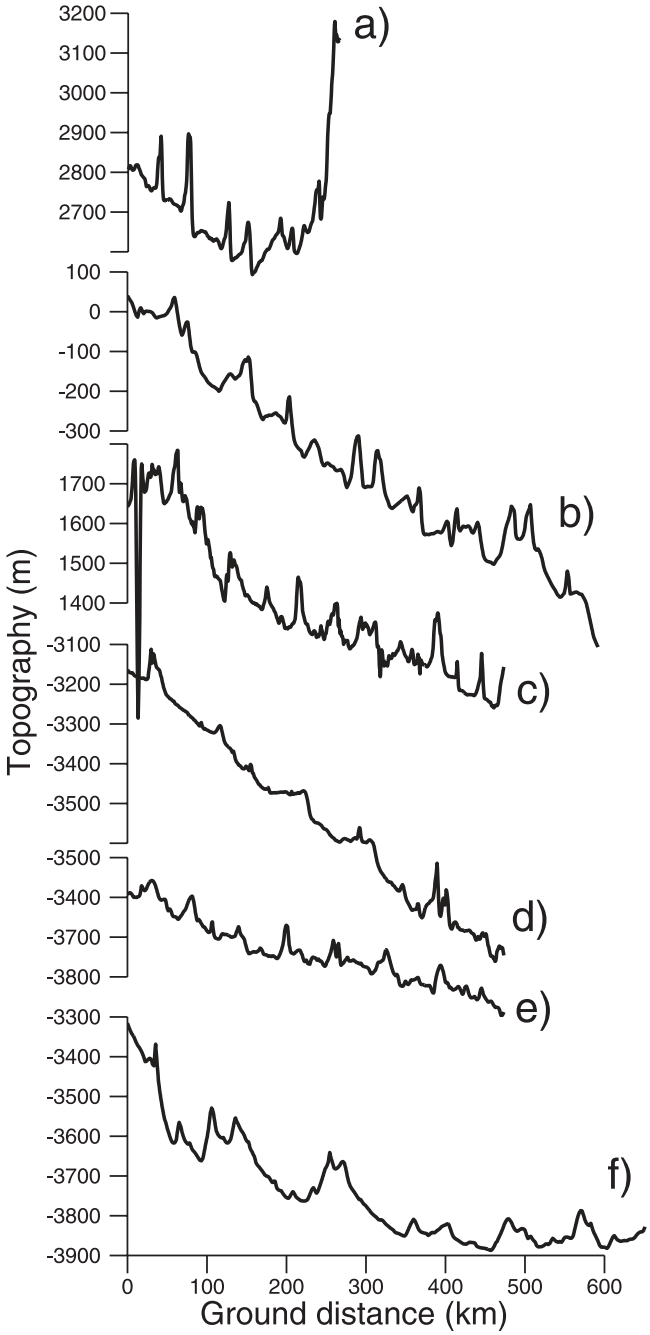

Figure 4. Topographic profiles taken across wrinkle ridges in a) Solis Planum, b) Lunae Planum, c) Hesperia Planum, d) Alba Patera, e) Arcadia Planitia, f) Chryse Planitia. The location of the profiles is indicated in Figures 3 and 5. Data from *Smith et al.* [2001].

lying individual ridges penetrate tens of kilometers deep in the lithosphere and dip systematically to the same direction across the plains [*Golombek et al.*, 2001]. A significant fraction of the current topography may reflect reverse motion on the stacked faults. *Golombek et al.* [2001] interpreted that topography as indicative of faults dipping toward the high-standing topography. On the other hand, *Okubo and Schultz* [2001] favored faults dipping in the opposite direction on the basis of a model that assumes internal deformation of fault-bounded blocks.

[12] More recent analyses [*Okubo and Schultz*, 2002; *Tate et al.*, 2002] have documented faults in Solis and Lunae Plana that do not follow the consistent vergence advocated by *Golombek et al.* [2001]. However, there are domains in which faults dip consistently to the west, most notably in Solis Planum, near 277°E, 25°S (Figure 4a). East-dipping faults occur more randomly. In some cases, ridges occur in pairs, with opposite vergence (e.g., Figure 4b) and may reflect a near surface branching of the underlying thrust. Further studies that take into account fault length, inferred fault offset and proximity of other faults are needed to better understand the regional arrangement of wrinkle ridges. We will present in section 5 finite element models that show how faults dipping toward the high-standing area may be favored in presence of lateral variations of geotherms and/or crustal thickness.

[13] In Lunae Planum, topographic data show a second set of ridges trending east–west, nearly perpendicular to the trend detected in Viking images [*Montési*, 2002]. The most pronounced of these ridges are visible in Figure 3b, near 291°E and 11°N. These ridges are nearly invisible in the Viking and Mars Orbiter Camera (MOC) images because of the illumination direction and of the apparent lack of a summit crenulation. As the tectonically important feature of wrinkle ridges is the master fault, which is expressed by the ridge, and not the wrinkle [*Schultz*, 2000], these ''wrinkle-less'' ridges should be considered as bona fide examples of wrinkle ridges. The orientation of the second set of ridges in Lunae Planum is at odds with the Tharsis-dominated stress field that controls the nearly perpendicular N–S ridges [*Watters and Maxwell*, 1986]. They are also unlikely to represent buried craters, as other ridges in the Lunae Planum [*Plescia*, 1991; *Allemand and Thomas*, 1995]. Instead, the E–W ridges are circumferential to a topographic high at the southwest corner of Lunae Planum, near 5°N, 290°E; their orientation is controlled by a local stress field. The E–W ridges often end against a N–S ridge, indicating that they formed later. However, more detailed mapping of the ''wrinkle-less'' ridges should be conducted to address their relation to the classical wrinkle ridges. Hesperia Planum displays two perpendicular sets of ridges as well (Figure 3c), but the ridges are so intertwined that they probably formed contemporaneously [*Raitala*, 1988; *Mangold et al.*, 2000]. The spacing of each set of wrinkle ridges in Hesperia Planum is of order 40 km [*Watters*, 1991; *Goudy and Gregg*, 2002].

[14] Although largely featureless in Viking images, the northern plains of Mars appear riddled with linear features in MOLA topography [*Withers and Neumann*, 2001]. Although the first of these new ridges, to the north of Alba Patera (Figure 5a), were originally interpreted as ancient beach terraces [*Head et al.*, 1999], a more complete data set shows that these lineations are more consistent with degraded wrinkle ridges [*Withers and Neumann*, 2001; *Thomson and Head*, 2001; *Head et al.*, 2002]. Figure 5b shows another example of lowland ridges in Arcadia Planitia. Lowland ridges are subparallel and controlled both by global stresses such as the Tharsis province and local stress sources such as the Utopia basin [*Head et al.*, 2002]. The lowland ridges parallel and complete previously recognized ridge trends, implying a common origin and time of formation [*Head et al.*, 2002].

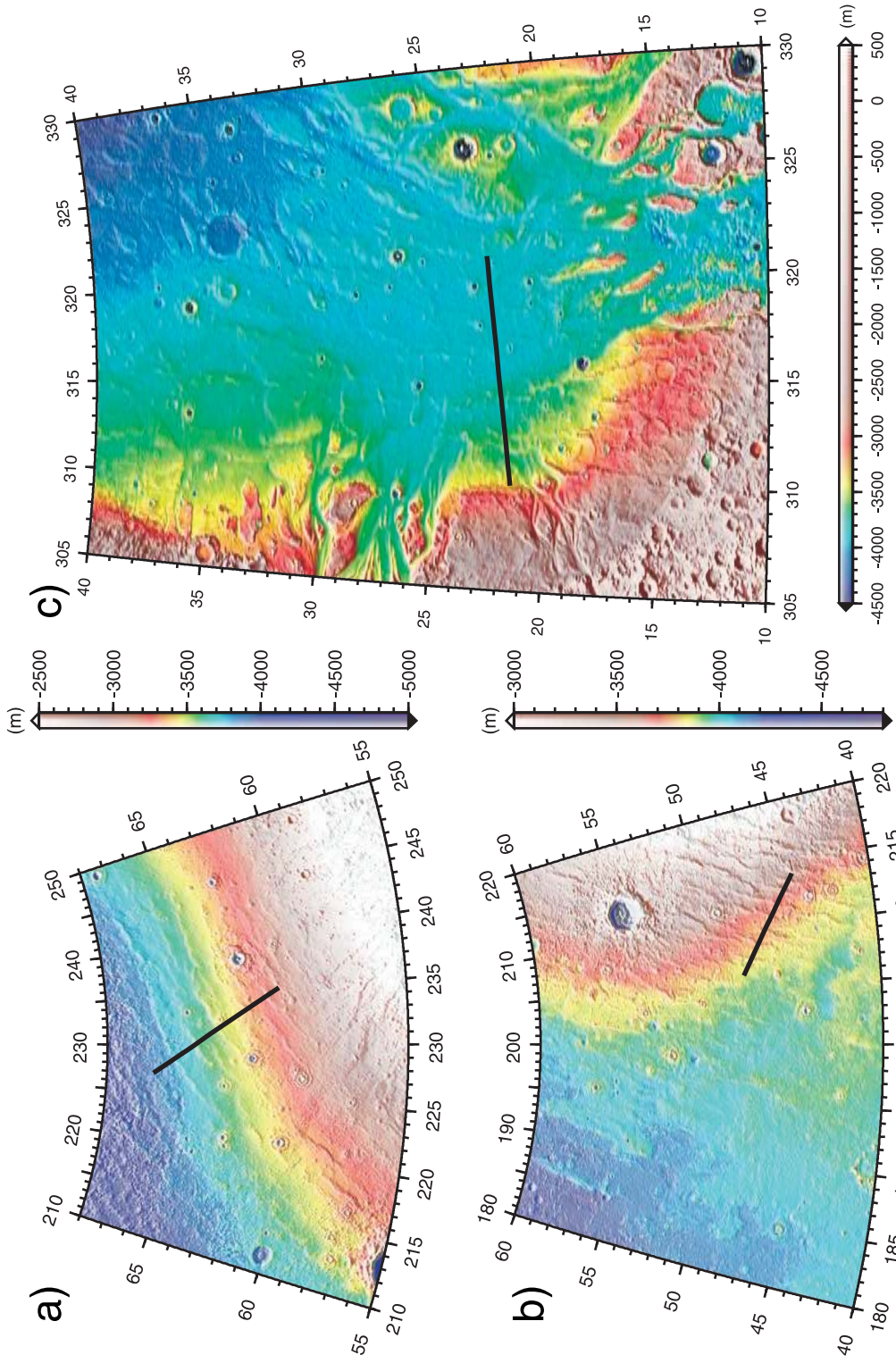

Figure 5. Digital Elevation Models of a) the northern flank of Alba Patera, b) south-east Arcadia Planitia, and c) Chryse Planitia. Terrain models from Mars Orbiter Laser Altimeter (MOLA) data gridded in $2' \times 1'$ blocks [*Smith et al.*, 2001].

[15] Northern lowlands ridges have a smaller height than the ridges recognized in Viking images, which, combined with the identification of buried impact structures and the unique roughness properties of the northern lowlands [*Aharonson et al.*, 1998; *Kreslavsky and Head*, 2000; *Aharonson et al.*, 2001], led *Head et al.* [2002] to infer that ~100 m of sediments covers a Hesperian-age northern plain similar to Lunae Planum in age and morphology. More evidence for significant flux of material toward the lowlands include possible buried channels in Chryse Planitia [*Zuber et al.*, 2000] and massive erosion in Arabia Terra [*Hynek and Phillips*, 2001]. Large parts of the northern plains have been imaged at high resolution. These images also indicate that sediments cover the northern plains [*Malin and Edgett*, 2001]. Although controversial, the northern ocean that has been proposed to have been in the Hesperian [*Head et al.*, 1999] could have facilitated the sediment deposition [*Baker*, 2001; *Jakosky and Phillips*, 2001]. These sediments are different from the older infilling of impact basins in the same region [*Frey et al.*, 2002].

[16] In addition to their degraded appearance, northern lowland ridges differ from the ridges in other ridged plains by a larger spacing, ~80 km, which may also reflect sedimentation of a preexisting ridged plain [*Head et al.*, 2002]. Interaction between sedimentation and ridges is also evident in Chryse Planitia (Figure 5c), where mass flow is guided by the ridges: the ridges are present in streamlined topographic highs and preexisting plains kipukas, especially near the mouth of the channels. Debris flows were guided by preexisting ridges. However, we will argue in section 6.2 that the sediment infilling has difficulties in explaining the difference in ridge spacing. Instead, we show that fault spacing may be controlled by a localization instability in a brittle layer of different thickness. The thickness of the brittle layer may reflect the different crustal thickness between the northern lowlands and the other ridged plains [*Zuber et al.*, 2000] (Figure 1b).

3. Localization Instability

[17] The spacing or wrinkle ridges varies systematically between the northern and southern hemisphere. Using the theories of buckling and localization instabilities, we can link ridge spacing to the strength profile of the Martian lithosphere [*Biot*, 1961; *Fletcher and Hallet*, 1983; *Montési and Zuber*, 2003a]. These theories, being semi-analytical, permit the exploration of a wide range of parameters describing the Martian lithosphere. However, they are valid only for the onset of the instability, not once ridges are well formed, and they neglect a host of complications realistically present in the lithosphere, such as preexisting structures and lateral variations in lithosphere properties. To handle these, numerical techniques are required. In this section, we use the instability analysis to provide a simplified picture of the lithosphere in the Martian highlands and lowlands, and in the next section, we use a finite element model to show what is the effect of a regional gradient in the structure of the lithosphere.

3.1. The Buckling and Localization Instabilities

[18] A model lithosphere with vertically stratified mechanical properties deforms by pure shear as long as the interfaces between different mechanical layers are perfectly flat and horizontal. However, any topography at these interfaces generates a secondary flow that in turn deforms the interfaces [*Fletcher*, 1974; *Smith*, 1977; *Johnson and Fletcher*, 1994]. The rate at which interface perturbations grow varies as a function of the perturbation wavelength. The growth rate may be maximum, or diverge at particular wavelengths, which may be expressed in the tectonic record [*Biot*, 1961; *Johnson and Fletcher*, 1994]. Lithospheric-scale instabilities are associated with these wavelengths.

[19] Two simultaneous instabilities develop when the lithosphere is subjected to horizontal shortening. One of them, the buckling instability, results in broad undulations of the lithosphere as a whole, with wavelength λ_B [*Fletcher*, 1974; *Ricard and Froidevaux*, 1986; *Zuber*, 1987; *Zuber and Aist*, 1990]. The other, the localization instability, results in periodically spaced localized zones of high deformation rate, that we interpret as faults [*Montési and Zuber*, 2003a]. The wavelength of that instability, λ_L, gives the fault spacing. The buckling instability might also produce regularly spaced faults if the undulations reach sufficient amplitude to produce significant stress heterogeneities before the fault pattern develops [*Martinod and Davy*, 1994; *Montési and Zuber*, 2003b].

[20] These two instabilities do not require exactly the same type of mechanical layering in the lithosphere. Buckling requires a strong layer overlying a weaker substrate [*Fletcher*, 1974; *Smith*, 1977] and is favored if the strong layer is plastic. For tectonic applications, that layer may be identified with the brittle upper crust or upper mantle [*Fletcher and Hallet*, 1983; *Zuber*, 1987]. In contrast, the localization instability requires a layer where faulting occurs, but it can be stronger or weaker than its substrate. In this study, the localizing layer is also identified with the brittle upper crust or mantle, but it is possible that it is only a part of it [*Montési and Zuber*, 2003b].

[21] Beyond its strength σ or its apparent viscosity η, the rheology of a layer is characterized by the effective stress exponent n_e, a measure of the response of the overall strength of a material to a local perturbation of, for instance, the strain rate $\dot{\varepsilon}$ [*Smith*, 1977; *Montési and Zuber*, 2002]. The effective stress exponent is defined as:

$$\frac{1}{n_e} \equiv \frac{\dot{\varepsilon}}{\sigma}\frac{\mathrm{d}s}{\mathrm{d}\dot{\varepsilon}}. \tag{1}$$

If $n_e > 1$ (non-Newtonian behavior), increasing the strain rate decreases the apparent viscosity but not the strength of the material; the material is stable with respect to local perturbations. This is the case for rocks deforming in the dislocation creep regime. A material is termed plastic in the limit $n_e \to \infty$ [*Chapple*, 1978; *Smith*, 1979; *Fletcher and Hallet*, 1983; *Zuber and Aist*, 1990], or, more conveniently, $1/n_e \to 0$. When $n_e < 0$, the material weakens dynamically: a local increase of strain rate decreases not only the apparent viscosity but also the strength of the material. Hence the material is unstable with respect to local perturbations of strain rate and generates spontaneously localized shear zones that we identify with faults [*Montési and Zuber*, 2002].

[22] While generated by local perturbations, these localized shear zones organize at the scale of the lithosphere into regularly spaced fault sets as they interact with one another and with the nonlocalizing layers of the lithosphere [*Montési and Zuber*, 2003a]. The lithospheric-scale fault pattern is controlled by the localization instability. The morphology of the ridges cannot be addressed with this analysis as the perturbations are infinitesimal, and near-surface interbed slip is not modeled.

3.2. Instability Scaling

[23] Both buckling and localization instabilities may result in regularly spaced ridges [*Montési and Zuber*, 2003b], but they differ in the relation between ridge spacing and brittle layer thickness that they predict [*Montési and Zuber*, 2003a]. Physically, the wavelength of each instability is controlled by a resonance between certain deformation modes within the strong and/or localizing layer. The resonances involved in the buckling and localization instabilities are different in detail, and have different associated wavelengths, which can be determined analytically [*Montési and Zuber*, 2003a]. Resonances occur at any integer multiple of a fundamental wavenumber. We define j as that integer, and call it the order of the resonance and of the associated buckling or localization instability. The resonant wavelengths are the basis for a scaling relation between the instability wavelength, λ_L and λ_B, the thickness of the strong and/or localizing layer H, and the effective stress exponent of that layer, n_e.

[24] For the buckling instability, we obtain

$$\frac{\lambda_B}{H} = \frac{2}{1/2 - a_B} \times \left(1 - \frac{1}{n_e}\right)^{1/2}, \tag{2}$$

and for the localization instability, we have

$$\frac{\lambda_L}{H} = \frac{2}{a_L} \times \left(-\frac{1}{n_e}\right)^{1/2}, \tag{3}$$

where a_B and a_L are the spectral offsets, which depend on the type of strength profile assumed in the lithosphere. In *Montési and Zuber* [2003a], we have calibrated a_B and a_L for the cases where the strength of the layer increases with depth and the strength of the substrate decreases quasi-exponentially, as may be expected if there is only one brittle and one ductile layer in the lithosphere. We found

$$0 < a_B < 1/4, \tag{4}$$

$$1/4 < a_L < 1/2. \tag{5}$$

The density of the lithosphere has little effect on the localization instability, but reduces the maximum growth rate and the preferred wavelength of the buckling instability. The order $j = 0$ gives the longest preferred wavelength for each instability family, which we consider the most likely to be visible in nature. Higher order instabilities $j \geq 1$ may also be present, but are harder to differentiate from noise in the $j = 0$ instability. Hence we consider only $j = 0$ in the application to large-scale tectonics. For equal brittle layer thickness, the wavelength of the localization instability is generally smaller than that of the buckling instability (Figure 6).

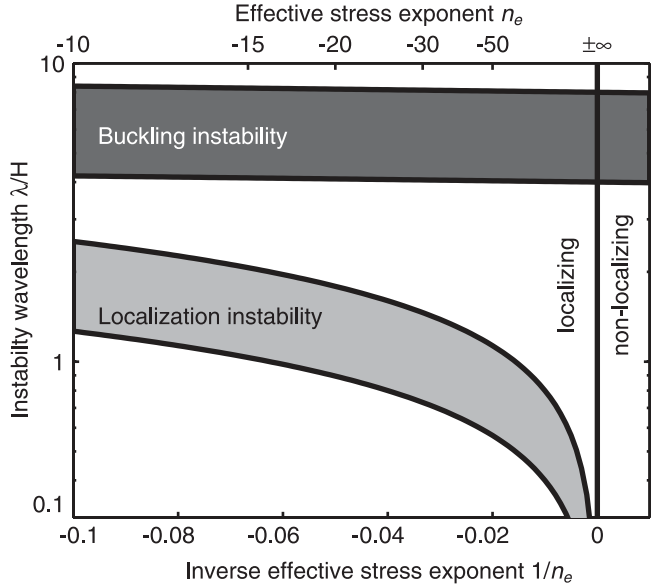

Figure 6. Wavelength of the buckling and localization instabilities as a function of the effective stress exponent. The parameter H is the thickness of the material that develops the instability. Localization requires $n_e < 0$ and is more efficient for more negative $1/n_e$. The range of wavelengths for each instability corresponds to the range of a_B and a_L in equations (2) and (3).

[25] The effective stress exponent that applies to the Martian lithosphere cannot be specified a priori because the exact localization mechanism is not known, and because extrapolating the values determined from laboratory studies requires reasonable caution. On the basis of rock mechanics experiments, the effective stress exponent may be between -10 to -50 for brittle failure mechanisms, and between -300 and -50 for localization over preexisting faults [*Montési and Zuber*, 2002]. The same localization process is probably at work in the ridged plains and in the northern lowlands, as similar tectonic structures, the wrinkle ridges, are observed in these areas. Hence we may assume that n_e, although unknown, is identical in both regions.

[26] Table 1 shows what thickness of strong or localizing layer is needed to explain the ridge spacing in the ridged plains or in the northern lowlands according to each instability. The values $n_e = -50$ and $n_e = -15$ are chosen to illustrate the possible wavelengths of the localization instability. If the localization instability controls the ridge spacing, $n_e = -15$ and $a_B = 1/4$, the thickness of the layer undergoing localization may be between 40 and 80 km in the highlands and twice that much in the lowlands. For tighter constraints on the depth of localization, we must compute the growth spectra of realistic strength models, which do not assume an a priori value for the spectral offsets a_B and a_L.

3.3. Growth Spectrum

[27] Because the spectral offsets (a_B and a_L) in equations (2) and (3) were determined empirically for simplified models of the lithosphere [*Montési and Zuber*, 2003a], we need to verify the prediction of instability wavelengths for

Table 1. Inferred Depth of Brittle-Ductile Transition

Ridge Spacing	Ridged Plains 40 km	Northern Lowlands 80 km
Bucking instability	5 to 10 km	10 to 20 km
Localization instability, $n_e = -50$	70 to 141 km	141 to 282 km
Localization instability, $n_e = -15$	38 to 77 km	77 to 144 km

more realistic models of the Martian lithosphere. This also results in a tighter range of H compatible with a given effective stress exponent n_e. Hence we compute the growth spectra using strength profiles derived from laboratory experiments on rock deformation.

[28] Following the method described by *Montési* [2002] and *Montési and Zuber* [2003b], the lithosphere is idealized as a sequence of horizontal layers (Figure 7). The density and dominant rheology are specified for each layer. The dominant rheology is the weakest of the pressure-dependent brittle strength and temperature-dependent ductile creep law. The brittle strength follows Byerlee's law of frictional sliding [*Byerlee*, 1978], which does not depend on rock type. By contrast, the ductile flow law does depend on the rock type. Meteorites as well as in situ analyses of Martian rocks indicate that the crust is composed mostly of igneous rocks. Although andesite-like compositions have been recognized [*McSween et al.*, 1999; *Bandfield et al.*, 2000], most analyses indicate a basaltic composition for the crust [*McSween*, 1994; *Zuber*, 2001; *Wyatt and McSween*, 2002]. Hence we use the dislocation creep laws of diabase [*Caristan*, 1982] for the crust. The upper mantle is probably olivine-rich [*Longhi et al.*, 1992; *Zuber*, 2001] and may be dry if the crust is extracted from it by partial melting [*Hirth and Kohlstedt*, 1996]. *Hauck and Phillips* [2002] argue that water extraction on Mars is not efficient, so that a wet olivine rheology is appropriate for the Martian interior. While this may be true for the average mantle composition, we are concerned here only with the shallowest mantle, which is most likely to have undergone melting and water extraction. We envision that the Martian lithospheric mantle is drier than the interior. Hence we use the rheology of dry olivine [*Karato et al.*, 1986] for the mantle. The depth at which these flow laws are weaker than the brittle failure envelope is shown in Figure 8.

[29] The ductile strength is a nonlinear function of the strain rate. Obviously, there is no direct constrain on the strain rate at the time of ridge formation. Here we select a strain rate of 10^{-16} s^{-1}, slightly smaller than in terrestrial diffuse plate boundaries [*Gordon*, 2000]. The thickness of the layers in the model used to compute the growth spectra as well as the depth-dependent strength profile in the ductile regime are computed for a prescribed temperature profile [*Montési and Zuber*, 2003b]. We assume that the temperature increases linearly with depth to a saturation temperature of 1350°C similar to that of the Earth's asthenosphere. At the surface, we assume a temperature of −20°C, warmer than present-day Mars, but consistent with models of the Martian atmosphere at the time of ridge formation [*Carr*, 1999]. The surface temperature has only a weak influence on the preferred instability wavelengths. The effective stress exponent of the ductile layers is given by the flow law. In the brittle regime, we only constrain n_e to be the same for the brittle crust and the brittle mantle. Localization requires $n_e < 0$. From the scaling analysis, $n_e \sim -15$ should explain the ridge spacing.

[30] Stokes' equation is solved in each layer and stress and velocity boundary conditions are matched to determine the growth rate of interface perturbations as a function of their wavelength, or growth spectrum. The buckling instability appears as a finite maximum of growth rate, and results in smooth undulations of the brittle layers as a whole. The growth rate diverges at the localization instability, reflecting the unstable character of localization [*Montési and Zuber*, 2003a].

[31] The growth spectra of models with 30- and 60-km-thick crust are presented in Figure 9, along with the corresponding strength profiles. We used $n_e = -16$ and dT/dz = 12 K.km^{-1}. Under these conditions, the 30-km-thick crust, corresponding to the northern lowlands, is brittle throughout (Figure 9c). The localization instability is marked by divergent growth rate at an ~90-km wavelength, similar to the spacing of ridges in the lowlands. With a 60-km-thick crust, as in Solis Planum, the localization instability has a wavelength of 40 km, similar to the ridge spacing in that region. The spectral offset is $a_L = 1/4$, consistent with the scaling derived in *Montési and Zuber* [2003a]. In the thick crust case, the upper mantle is surrounded by weaker material. Hence the strong upper

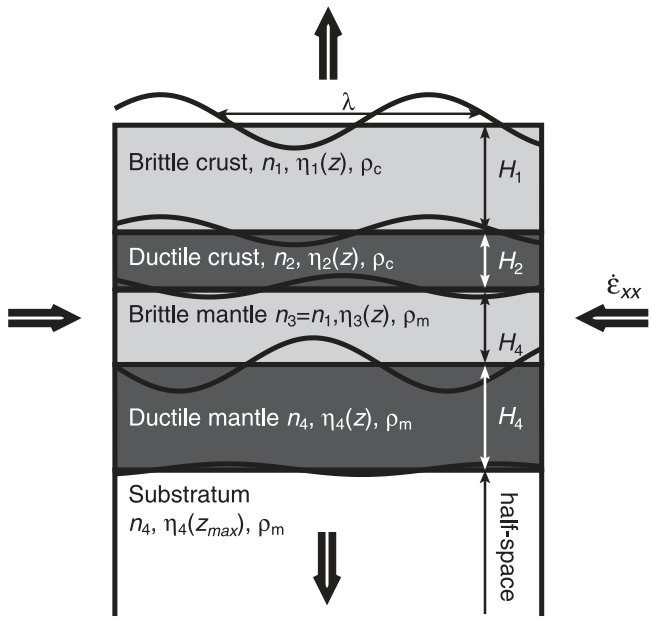

Figure 7. Schematic representation of lithosphere models. A sequence of layers undergoes horizontal shortening. The strength profile follows the weakest of frictional resistance or ductile flow law. Each layer i is characterized by a density ρ_i, a thickness H_i, an effective stress exponent n_i, and a viscosity profile $\eta_i(z)$ that correspond to the dominant deformation mechanism in that depth range. A substratum with rheology corresponding to the lowest level of the model is included for convenience. The shading differentiates between localizing layers (lighter shade, $n_i < 0$) and ductile layers (darker shade, $n_i \geq 0$). The same shading is used in the strength profile in the next figures. The ductile crust and brittle mantle are included only if the crustal thickness and geotherm allows it.

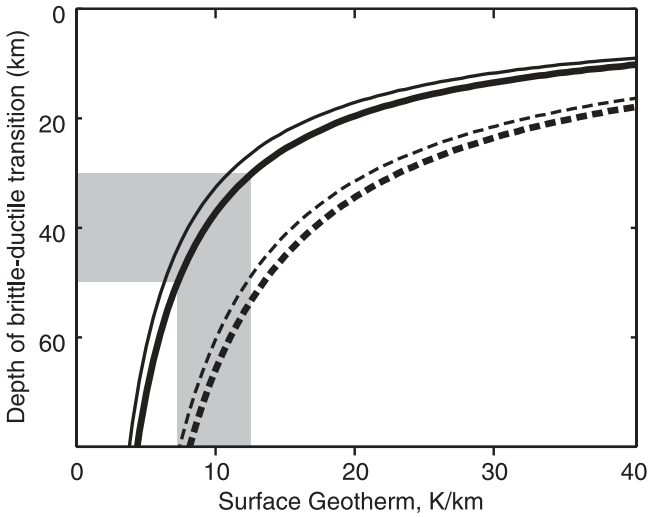

Figure 8. Depth of brittle-ductile transition for different materials as a function of the surface geotherm. Solid lines: diabase rheology [*Caristan*, 1982]; dashed lines: dry olivine [*Karato et al.*, 1986]; thick lines: strain rate 10^{-15} s^{-1}; thin lines: strain rate 10^{-18} s^{-1}. The brittle-ductile transition is defined as the point where the resistance to frictional sliding [*Byerlee*, 1978] equals the ductile strength. Horizontal shortening and a temperature profile in erf(z) with surface temperature of -20°C and asymptotic temperature of 1350°C are assumed.

mantle can buckle, as indicated by the broad maximum of growth rate around 75-km wavelengths. However, this mode of deformation has very little expression at surface, and a moderate growth rate of order 10. This deformation mode has not been recognized in the tectonics of Solis Planum.

[32] As localization becomes less efficient ($1/n_e \rightarrow 0^-$), more faults are needed to accommodate the deformation imposed over a given distance. Correspondingly, the wavelength of the localization instability decreases (Figure 10). Constraining the ridge spacing to be 40 or 80 km, there is a tradeoff between n_e and the geotherm, which controls the depth to the BDT (Figure 11). Indeed, a shallower BDT results in a longer λ/H to be modeled, which is achieved by increasing the efficiency of localization, or decreasing $1/n_e$. The 40-km ridge spacing in Solis Planum can be modeled by $n_e = -13$ if $dT/dz = 15$ K.km^{-1}, or $n_e = -25$ if $dT/dz = 7$ K.km^{-1}. For similar conditions, the ridge spacing in the northern lowlands is 80 to 90 km. In all these cases, localization is more efficient than expected for frictional velocity weakening, but is consistent with localization by other processes such as the loss of cohesion upon failure [*Montési and Zuber*, 2002].

4. Application to Wrinkle Ridge Spacing

[33] If buckling controlled ridge spacing, the faults underlying Martian ridges would not necessarily penetrate deeply into the lithosphere. They would be limited by the thickness of the strong buckling layer, which would be at most 10 km thick in the highlands ridged plains and a factor of two thicker in the lowlands (Table 1). In both locations, this is less than the crustal thickness inferred from MGS data [*Zuber et al.*, 2000] (Figure 1). First, we will assume that the thickness of the strong layer is limited by the brittle-ductile transition (BDT) of crustal rocks. The BDT is a function of the rock type and the geotherm (Figure 8). Then, we will explore the possibility that the strong layer reflects intracrustal stratification. Finally, as neither of these possibilities is likely to explain the systematic ridge spacing difference between ridged plains and northern lowlands, we explore the possibility that the ridge spacing is controlled by the localization instability. Then, the different crustal thickness between the highlands and the lowlands provides an explanation for the different ridge spacing.

4.1. Brittle-Ductile Transition Controlled by Different Geotherms

[34] If the ridge spacing is controlled by the buckling instability and the crust has similar composition in the highlands and the lowlands, then the ridge spacing implies

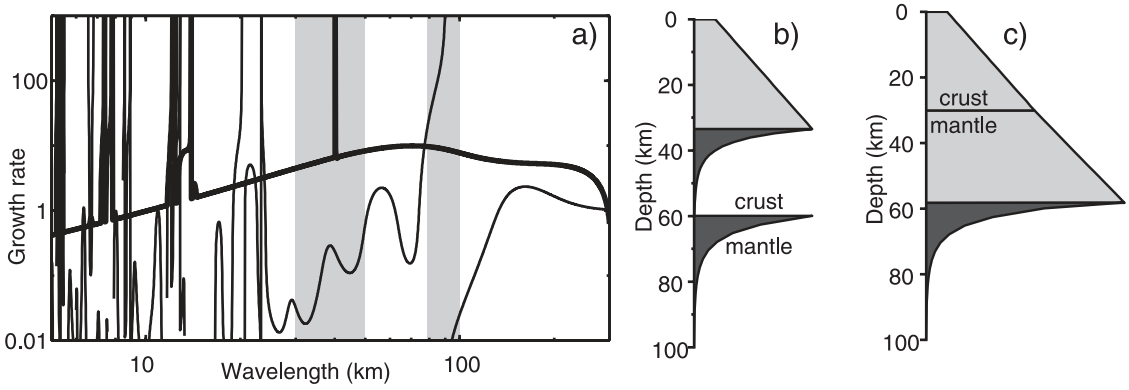

Figure 9. a) Growth spectra of the lithosphere models for Solis Planum (thick line, 60-km-thick crust) and the northern lowlands (thin line, 30-km-thick crust). Strength profiles for the models of b) Solis Planum and c) the northern lowlands. The geotherm is 12 K.km^{-1} and $n_e = -16$ in the brittle regime in both cases. The shaded regions in a) show the range of ridge spacing in Solis Planum (30 to 50 km), and the northern lowlands (80 to 100 km). The spikes in the growth spectra indicate the localization instability.

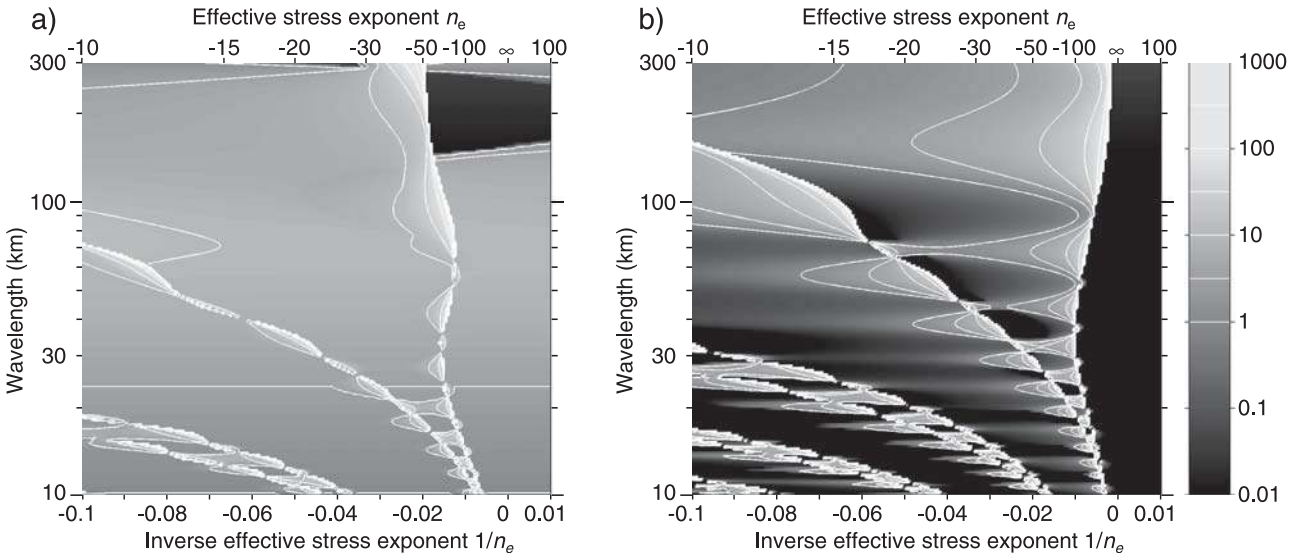

Figure 10. Map of growth rate as a function of effective stress exponent of localizing layer and perturbation wavelength for a lithosphere with a) a 60-km-thick crust (as in Solis Planum, Figure 9b) and b) a 30-km-thick crust (as in the northern lowlands, Figure 9c). High growth rate is in lighter tones. The localization instability is identified by the chains of very high growth rate. These graphs give the wavelength of the instability as function of the effective stress exponent.

that the geotherm in the lowlands was at least a factor of two lower than in the ridged plains at time of ridge formation. However, this situation is unlikely. The ridges formed roughly at the same time in both areas [*Head et al.*, 2002], and the northern lowlands lithosphere is approximately as old as the Martian highlands [*Frey et al.*, 2002], precluding significant differences in the mantle heat flow or in the heat loss by cooling of a immobile lithospheric plate between the two regions. The lowlands' lithosphere might have lost heat more rapidly than the highlands during an early episode of plate tectonics in the lowlands [*Sleep*, 1994]. However, it is not known how strong the heat flux

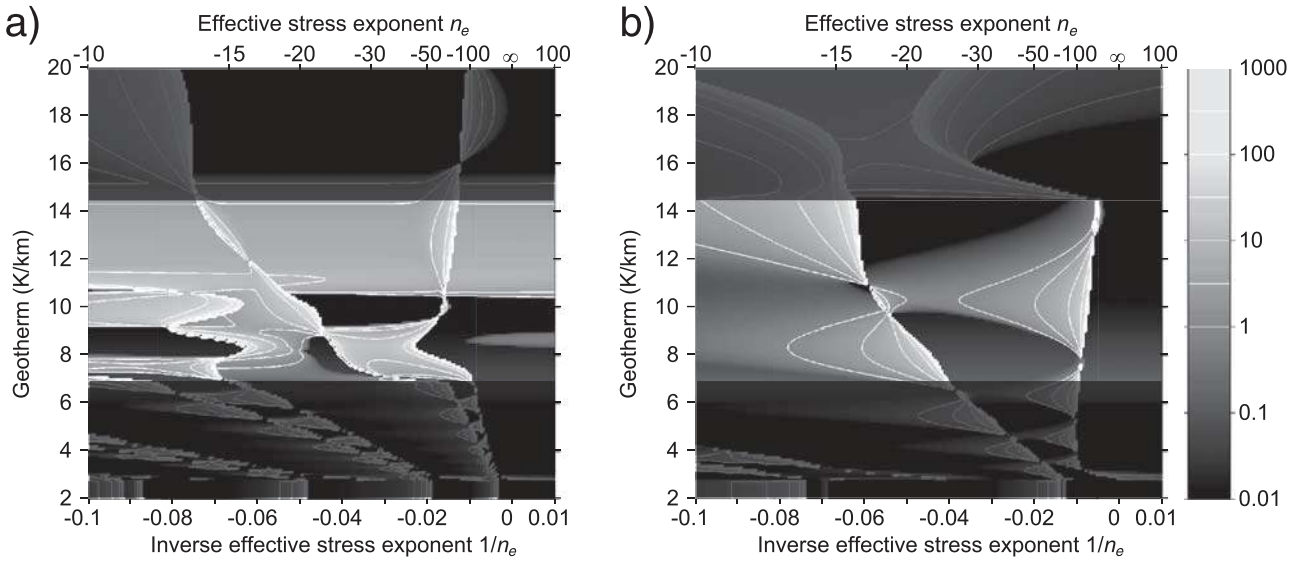

Figure 11. Map of growth rate as a function of effective stress exponent of the localizing layers and geotherm for a) a perturbation wavelength of 40 km and a lithosphere with a 60-km-thick crust (as in Solis Planum, Figure 9b) and b) a perturbation wavelength of 80 km and a lithosphere with a 30-km-thick crust (as in the northern lowlands, Figure 9c). High growth rate is in lighter tones. The localization instability is identified by the chains of very high growth rate. These graphs give the geotherm needed to match the ridge spacing as a function of the effective stress exponent. The shaded parts of the graph indicate the range of geotherms for which the ridge spacing in both the highlands and the lowlands cannot be matched with a similar n_e.

reduction would be, and for how long it would be preserved with a dynamic mantle. In addition, the recognition of buried impact basins [*Smith et al.*, 1999; *Frey et al.*, 2002; *McGill*, 2001; *Thomson and Head*, 2001] makes it unlikely for plate tectonics to have occurred in the lowlands after the end of heavy bombardment. Degree-1 convection that caused excess heat loss and resurfacing in the lowlands [*Zhong and Zuber*, 2001] would cause lowland ridges to have smaller spacing than in the highlands, which is contrary to the observations.

[35] It is possible that the lithospheres of Solis and Lunae Plana were reheated by mantle plumes and associated volcanism, but the temperature anomaly associated with thermal plumes on Earth is at most 200 K [*Shen et al.*, 1998; *Korenaga and Kelemen*, 2000], or 20% of the temperature drop across the lithosphere. If a similar temperature change also happened on Mars, it would not be sufficient to explain the difference of depth of BDT. Radiogenic heating in the thicker highland crust, also cannot account for more than 2.1 $K.km^{-1}$, assuming a concentration of heat-producing elements in the Martian lower crust similar to that of tholeiitic basalts on Earth 3 Gyr ago [*Turcotte and Schubert*, 1982].

[36] For simplicity, we assume the same surface temperature in the lowland and the highlands. In fact, the mean temperatures at present varies from $-120°C$ near the poles to $-50°C$ near the equator. The best studied ridged plains are near the equator (Figure 1) and on average less cold than the lowland plains. This might have been the case at the time of ridge formation as well. However, surface temperature differences of even 100°C result in only a few kilometers of difference in the BDT, and therefore in the wavelength of the buckling instability. This is insufficient to account for the factor of two difference in ridge spacing between the highlands and lowlands.

[37] In summary, there is little reason to expect a significant difference between the thermal structure of the lowlands and the highlands during ridge formation, but future thermal models should explore this question in more detail.

4.2. Brittle-Ductile Transition Controlled by Different Crustal Composition

[38] The factor of two difference in BDT implied by the buckling analysis may reflect different crustal compositions between the highlands and the lowlands. Data from both Mars Pathfinder and Mars Global Surveyor Thermal Emission Spectrometer (MGS-TES) indicate the presence of silica-rich rocks such as icelandite or andesite [*McSween et al.*, 1999; *Bandfield et al.*, 2000]. *Bandfield et al.* [2000] showed that the andesite-like component to be predominant in the northern lowlands. Although compositional inferences made from remote sensing data are nonunique and sediments make the link between surface and crustal composition ambiguous, especially in the lowlands, MGS-TES data are consistent with the Martian crust being more silica-rich in the lowlands than the highlands. However, silica-rich rocks such as granite are generally weaker than basaltic rocks such as gabbros [*Tsenn and Carter*, 1987; *Evans and Kohlstedt*, 1995]. Hence, if that compositional difference is real, the BDT of the lowlands would be shallower than in the highlands, for identical geotherm, which would result in more closely spaced ridges in the lowlands, contrary to the observations [*Head et al.*, 2002]. It may be argued that the lowland crust is actually more mafic than the highland crust but is covered by a veneer of silica-rich sediments derived from the highlands. In this case, the density difference between highlands and lowlands could explain their elevation difference in the same manner as the different elevation of the oceanic and continental crusts on Earth and the BDT in the highland crust would be shallower than that of the lowland crust. However, one would expect the surface of the highlands to be silica-rich, contrary to the remote sensing observations [*Bandfield et al.*, 2000]. The spectral signature of the lowlands sediments is also compatible with that of weathered basalt [*Noble and Pieters*, 2001; *Wyatt and McSween*, 2002], which is easier to reconcile with their geographic distribution. Unless the crust of either the lowlands or the highlands is dominated by a different rock type than seen at the surface, or the geotherm of the lowlands is much colder than that of the highland, for a unknown reason, the BDT of the lowlands is unlikely to be a factor of two deeper than in the highlands. Hence the ridge spacing, if controlled by the buckling instability, does not reflect the BDT of crustal materials.

4.3. Buckling Controlled by Intracrustal Stratification

[39] The buckling layer may be limited by a change of rock type with depth within the crust rather than the BDT. Early models of ridge spacing assumed that the strong layer corresponds to basaltic flood plain units that are underlain by a weaker substrate usually identified with a lunar-type megaregolith [*Saunders et al.*, 1981; *Zuber and Aist*, 1990; *Watters*, 1991]. Recent morphological studies of canyon walls showed that the plain's thickness is at least 8 km [*McEwen et al.*, 1999; *Caruso and Schultz*, 2001; *Peulvast et al.*, 2001], which is inconsistent with previous models using viscoelastic buckling requiring plain thicknesses of order 1 km [*Saunders et al.*, 1981; *Watters*, 1991]. Models using a plastic layer [*Zuber and Aist*, 1990] are consistent with such a plain thickness. However, they also imply that the Hesperian plains unit would be between 20 and 40 km thick in the lowlands to explain the longer ridge spacing (Table 1). The plains would then constitute the major part of the 20- to 30-km-thick crust of the lowlands [*Zuber et al.*, 2000] (Figure 1), which is inconsistent both with the identification of basins underneath the volcanic plain unit in the lowlands [*Frey et al.*, 2002] and with the presence of a significant megaregolith underneath the volcanic plains, as needed for buckling. A weak substrate would also decouple efficiently the surface from deeper stresses [*Zuber*, 1995], which is hard to reconcile with observations of consistent ridge orientation over thousands of kilometers.

[40] In summary, it is unlikely that the buckling instability controls the ridge spacing, regardless of whether the buckling layer is limited by the brittle-ductile transition of the crust, or an intracrustal weak layer. We are thus motivated to test the hypothesis that ridge spacing is controlled by the localization instability. In that scenario, the thickness of the faulting layer is at least 40 km, depending on the value of effective stress exponent (Table 1). This value is consistent with the flexural rigidity

derived from flexural modeling of Solis Planum [*Zuber et al.*, 2000].

4.4. Ridge Spacing Controlled by the Localization Instability

[41] If the ridge spacing is controlled by the localization instability, H corresponds to the depth of faulting, which is indicated by the BDT of the lithosphere. As we discussed above, difference in the thermal or chemical structure of the crust are not sufficient to deepen the BDT by a factor of two in the lowlands, unless the crust has unusual compositions or these regions have undergone very different thermal evolutions. However, it is possible that the BDT is controlled by the mantle rheology in the lowlands and the crustal rheology in the highland ridged plains, because of the difference of crustal thickness [*Zuber et al.*, 2000] (Figure 1).

[42] As argued in section 3.3, the rheology of dry olivine [*Karato et al.*, 1986] provides a reasonable estimate of the strength of the mantle and the strength of the crust may be approximated by the strength of diabase [*Caristan*, 1982]. The diabase and dry olivine rheologies predict a factor of two deeper BDT in the mantle than in the crust for a given geotherm (Figure 8). Hence a thin crust, as in the lowlands, may be completely brittle, whereas a thicker crust, as in the highlands, may be ductile at depth. The same factor of two increase in the depth of the BDT can be obtained if the crust in the highlands is dominated by quartzite or granite, and the BDT of the lowlands is controlled by either dry diabase or wet olivine. However, these combinations of rock type are deemed less likely than the wet diabase/dry olivine pair assumed above for the reasons exposed in section 4.2.

[43] The geotherm is not necessarily the same in both regions: in the lowlands, the geotherm should be less than $\sim$15 K.km^{-1} for the 20- to 30-km-thick lowland crust to be completely brittle, whereas in the highlands, the geotherm must exceed 7 K.km^{-1} for the 60-km-thick crust of the Solis Planum to be ductile at its deepest levels. A higher geotherm in the highlands is needed if the 50-km-thick crust in Lunae or Hesperia Plana is to be ductile as well. If the highlands' geotherm is identical to that of the lowlands and is 11 $\pm$ 4 K.km^{-1}, the factor of two difference in ridge spacing between these regions is explained. Differences in geotherm between these areas would modulate this relation, but as argued above, they probably do not exceed 3 K.km^{-1}. The common geotherm implied by our analysis would change if a rock type different from diabase and dry olivine controlled the BDT in the Martian highlands and lowlands. For instance, if the rheology of the crust was controlled by quartzite [*Gleason and Tullis*, 1995], the implied geotherm would be less than 9 K.km^{-1} in the lowlands and more than 4 K.km^{-1} in the highlands. There is, however, no evidence for this rock type at the surface of Mars. The implied geotherms would also be lower if the surface temperature or the strain rate were higher than assumed here.

5. Finite Element Modeling of Regionally Consistent Fault Vergence

[44] Reliable topographic data from MOLA [*Smith et al.*, 2001] demonstrated that plains are vertically offset across ridges, indicating that individual ridges are underlain by deeply rooted faults [*Golombek et al.*, 2001] (Figure 4). The sense of the topographic offset indicates the dip direction, or vergence, of the fault. In some parts of Solis Planum, the faults dip consistently toward the high-standing area. The instability analysis presented above can match the predicted fault spacing, but cannot explain regionally consistent fault vergence. Indeed, if the region deforms by pure shear, conjugate faults are expected, with an approximately equal number of faults dipping toward and away from the high-standing areas. The symmetry of faulting can be broken if deformation has a component of simple shear in addition to the pure shear that represents horizontal shortening. We investigate using finite element models how such a component may arise from lateral variations in the mechanical properties of the lithosphere. Specifically, we model the effects of laterally varying crustal thickness and geotherm.

5.1. Numerical Technique

[45] The lithosphere is modeled as a visco-plastic material using the finite element method [*Chen and Morgan*, 1990; *Neumann and Zuber*, 1995; *Zuber and Parmentier*, 1996; *Behn et al.*, 2002]. The lithosphere is divided into contiguous elements that are initially rectangles. There are four nodes for each element. Velocity and forces are defined at each node of each element, and interpolated within the element. The physical relation between forces and velocities (or strain rate) is integrated over individual elements, so that each element is represented by an effective stiffness (or rather viscosity) matrix linking the velocity and the forces at each of its nodes. Then, displacement boundary conditions are imposed on selected nodes, so that, as the velocity in the model must be continuous and the forces at each node must be in equilibrium, it is possible to solve for the velocity and forces at every node [*Bathe*, 1996]. Our formulation is Lagrangian: computational nodes are advected with the velocity field. Concerns of finite distortion of the elements, time discretization, and regridding of the model are irrelevant for this work as we consider only the initial configuration of faulting.

[46] In the results presented herein, the computational domain is 600 km $\times$ 120 km, discretized in 300 $\times$ 40 rectangular elements. Each element is 2 km wide in the horizontal direction. From top to bottom, the mesh is composed of 30 rows of 2-km-high elements, 5 rows of 4-km-high elements, and 5 rows of 8-km-high elements. This stratification does not influence significantly the numerical results for the wavelengths of interest, but improves significantly the computation time.

[47] The top surface of the models is stress-free and the other boundaries have free-slip conditions. The vertical velocity is 0 at the bottom of the model and the horizontal velocity is 0 on the left wall and $U = -60$ km.Ma^{-1} on the right wall to provide the horizontal shortening rate of 10^{-7} yr^{-1} $\sim 3.16 \times 10^{-15}$ s^{-1}.

[48] The temperature, T, the pressure, P, and the strain rate, $\dot{\varepsilon}$, of each element are used to compute the stress required for ductile creep, σ_d, and its brittle strength, σ_b. The weakest of σ_d and σ_b is retained to compute the apparent viscosity of the element, $\eta = \min\{\sigma_d, \sigma_b\}/2\dot{\varepsilon}$, which is used to compute the stress and velocity fields in the model.

[49] The strain rate is initially uniform throughout the model, but is then recomputed from the velocity solution.

The procedure is repeated without deforming the model until self-consistent viscosity and strain rate fields are attained, producing the initial fault pattern that we discuss here. Convergence requires usually less than 200 iterations. In order to visualize the deformation field, we deform the grid producing the equivalent of 3% horizontal shortening in one time increment.

[50] The ductile flow law is

$$\sigma_d = B\dot{\varepsilon}^{1/n} \exp T_R/T, \tag{6}$$

where B, n, and T_R are constants determined from laboratory experiments and T the absolute temperature of an element. As before, we use the flow laws of dry olivine [*Karato et al.*, 1986] in the mantle and diabase [*Caristan*, 1982] in the crust.

[51] In the brittle regime, the rock strength follows Byerlee's law of frictional sliding [*Byerlee*, 1978]. Following *Neumann and Zuber* [1995], the brittle rock strength decreases with the logarithm of strain rate to simulate the dynamic weakening required for localization:

$$\sigma_b = (S + fP)\ (1 - C \ln \dot{\varepsilon}/\dot{\varepsilon}_0), \tag{7}$$

where S and f are experimentally determined constants, $\dot{\varepsilon}_0$ is a reference strain rate and C is a constant that controls the efficiency of localization. The dependence on strain rate mimics the velocity dependence of steady-state friction determined from laboratory experiments [*Dieterich*, 1979; *Ruina*, 1983]. The effective stress exponent in that regime is:

$$\frac{1}{n_e} = -\frac{C}{1 - C \ln \dot{\varepsilon}/\dot{\varepsilon}_0} \sim -C \tag{8}$$

For numerical reasons, localization requires $C > 0.1$, whereas we expect to match the ridge spacing for $C < 0.06$. Hence we do not address the question of ridge spacing with the finite element model but only that of the selectivity of fault vergence. Fault spacing is better addressed by the instability analysis of the previous section.

5.2. Results

[52] In the first model, there is no lateral variation of crustal thickness or geotherm (Figure 12a). The crustal thickness is 60 km, as in Solis Planum (Figure 1b). The temperature is 253 K at the surface, and increases with depth as erf(z) with a surface gradient of 10 K.km^{-1} and an asymptotic temperature of 1600 K. The crust is brittle to 40 km, and the mantle is brittle from 60 to 65 km (Figures 12a and 13a).

[53] Brittle failure, which is initially uniform (Figure 12a), collapses onto discrete bands of enhanced strain rate and reduced stress as the model converges to a self-consistent solution (Figures 14a, 14b, and 14c). The strain rate in the shear zones is about a factor of 10 higher than the strain rate of 10^{-7} yr^{-1} imposed on the model as a whole (Figure 14d). Between the bands, the strain rate is reduced to the point that the material is not undergoing failure (Figure 14c). The BDT deepens by a few kilometers beneath the shear zones due to the enhanced strain rate. Even deeper, in the ductile regime, the shear zones become diffuse. The power spectrum of the surface strain rate shows a pronounced maximum a wavelength of ~60 km (Figure 14e), corresponding to the spacing of localized shear zones, and a secondary maximum near 200 km. That secondary maximum may correspond to the buckling instability but is not well resolved in this model. As the model is laterally invariant, the pattern of localized shear zones is symmetric, with right-dipping and left-dipping faults of similar intensity (Figure 14d).

[54] In the second model, the crustal thickness varies from 60 to 54 km over the 600 km of the model (Figure 12b). As the weak lower crust is replaced by strong upper mantle, the strength of the lithosphere increases as the crustal thickness decreases (Figure 13b). The resulting fault pattern is asymmetric (Figure 15), with the strain rate being higher on faults dipping toward the thick crust region (Figure 15d). The spectrum of the surface strain rate (Figure 15e) shows a peak at the spacing of shear zones, around 70 km, and large amplitude at long wavelength that reflects a developing regional slope (Figure 15). The regional slope results from the lithosphere being weaker, and therefore deforming faster, where the crust is thick. The preferred faults dip toward the growing high-standing area.

[55] In the third model, the crustal thickness is 60 km throughout the model, but the surface geotherm decreases from 10 to 8.8 K.km^{-1} over the 600-km-wide model (Figure 12c). The deeper BDT where the geotherm is low results in stronger lithosphere (Figure 13c). As in the second model, the fault pattern is asymmetric, with the faults that dip toward the weak area being favored (Figure 16). The spectrum of the surface strain rate (Figure 16e) peaks at ~70-km wavelength. Its high amplitude at long wavelengths reflects the developing slope that, as in the second model, results from the lithosphere being weaker on one side of the model. The preferred faults dip toward the growing high-standing area.

5.3. Applications

[56] Gradients in crustal thickness and surface geotherm are both successful at producing an asymmetric pattern of faulting. The favored faults dip toward the weaker part of the lithosphere, being either of thicker crust or of higher geotherm. Shortening and thickening are concentrated in the weakest part of the model, resulting in progressive tilting of the surface, which may be part of the regional slope observed in Lunae and Solis Plana. This would be consistent with the observation that faults dip preferentially toward the high-standing areas [*Golombek et al.*, 2001].

[57] In Solis and Lunae Plana, lateral variations of geotherm similar to that considered in the third model may be linked to the Tharsis rise, if the volcano-tectonic province is due to mantle plumes. Solis Planum is best described as a local minimum of crustal thickness. Around 275°E, 24°N, where the systematic fault vergence is the most obvious, the crustal thickness increases toward the northwest, toward the high-elevation areas [*Zuber et al.*, 2000] (Figure 1b). The gradient of crustal thickness is comparable to that used above.

[58] Our models, which include only strain-rate weakening, do not eliminate completely the faults conjugate to the dominant vergence. Using either strain weakening, or

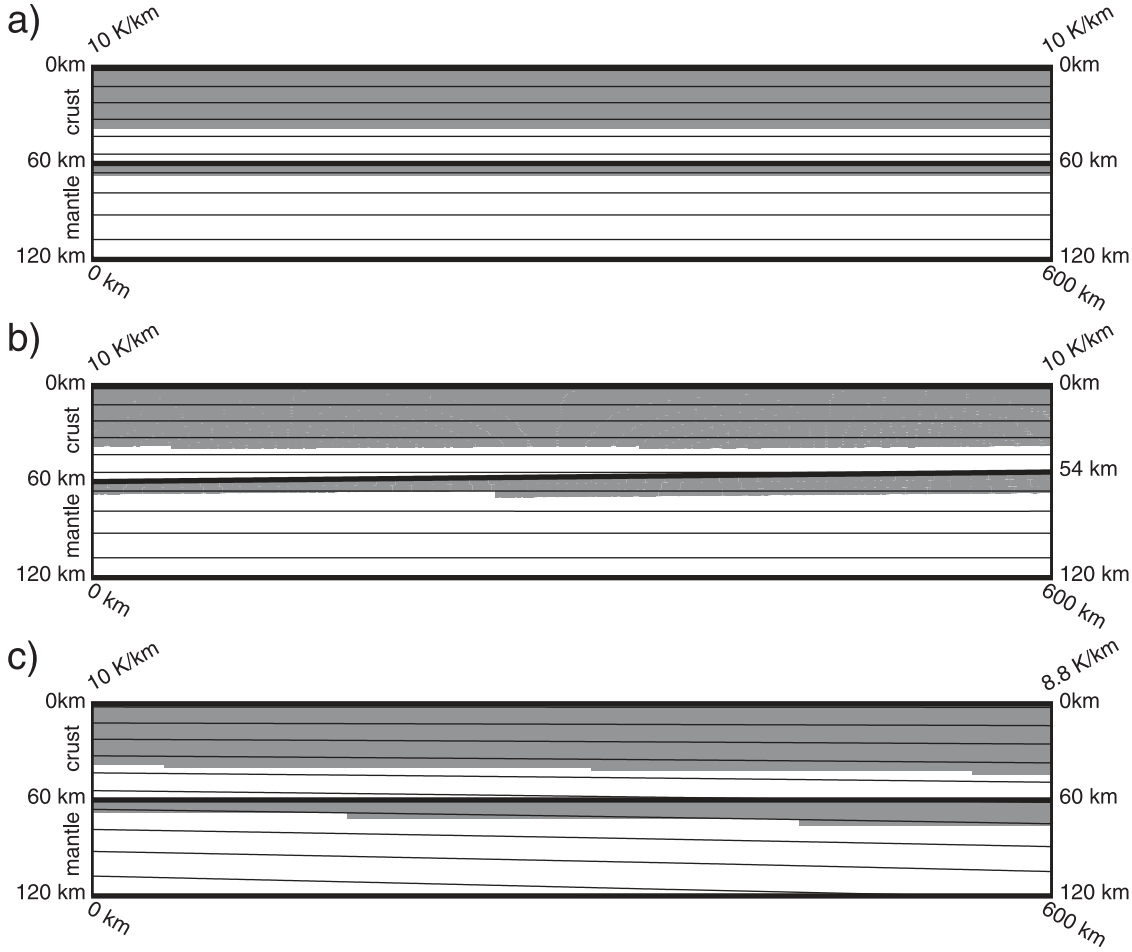

Figure 12. Initial configuration of finite element models. The thick line shows the base of the crust, and the thin lines represent isotherms every 100°C. The shaded region shows the elements undergoing failure if the model deforms under uniform strain rate. However, the failure zone changes and forms discrete shear zones after convergence of the model (Figures 14–16). a) no lateral gradients of crustal thickness and geotherm; b) lateral gradient of crustal thickness (1 km per 100 km); c) lateral gradient of geotherm (0.2 $K.km^{-1}$ per 100 km).

anisotropic weakening may force the least developed shear zones to be abandoned. Within our models, the asymmetry of faulting is enhanced if the crustal thickness or geotherm gradients are higher than shown here. However, this comes at the price of concentrating deformation to a region just a few tens of kilometers wide where the lithosphere is weakest. Awaiting improvements of the modeling technique, we conclude that vergence selectivity is possible for realistic lateral gradients of the crustal thickness or of the geotherm, although it remains to be determined whether this consistent vergence selectivity can occur over an entire ridged plain. It should be noted that recent studies found that both ridges dipping toward high-elevation areas and ridges dipping away from it are found in Solis and Lunae Plana, although the set dipping toward the high-elevation area is dominant in some areas [*Okubo and Schultz*, 2002; *Tate et al.*, 2002]. Our model can explain this observation even better than the original proposition that all the faults dip toward the high-elevation areas [*Golombek et al.*, 2001]. Time-dependent deformation in these models also reduces the selectivity of a given fault vergence, as a conjugate fault tends to form if displacement over an individual fault is too large.

6. Discussion

6.1. Fault Geometry Underneath Wrinkle Ridges

[59] The depth to which the faults underlying wrinkle ridges penetrate has been a major issue in Martian tectonics [*Plescia and Golombek*, 1986; *Watters*, 1991; *Golombek et al.*, 1991; *Watters and Robinson*, 1997]. Deep faulting models were recently promoted by the recognition of elevation offsets in MOLA data [*Golombek et al.*, 2001] and models of ridge morphology as folding driven by a deeper blind fault [*Schultz*, 2000]. Our models of ridge spacing, which make no a priori assumption about the depth of faulting, favor deep faulting as well. The comparison of ridge spacing in two different provinces leads us to conclude that faulting penetrates to the shallowest brittle-ductile transition (BDT) of the Martian lithosphere. In Solis and Lunae Plana, where the crust is 50 to 60 km thick, the BDT is determined from the crustal rheology and is 30 to 50 km

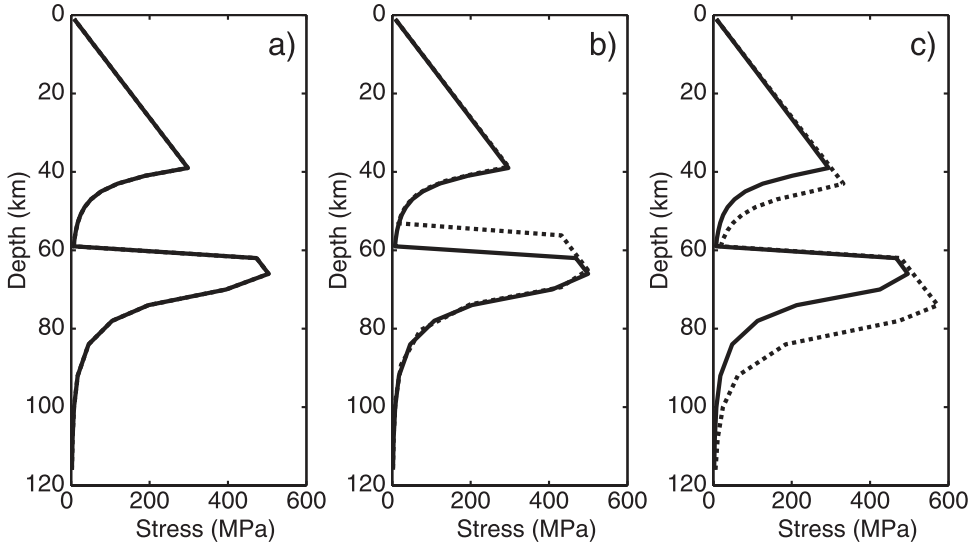

Figure 13. Stress supported in the left side (solid line) and right side (dotted line) of the finite element models before localization of the failure zones. The discretization of the profiles comes from the decomposition of the model into finite elements. The strength is given at the depth to the center of each element. a) no lateral gradients of crustal thickness and geotherm; b) lateral gradient of crustal thickness (1 km per 100 km); c) lateral gradient of geotherm (0.2 $K.km^{-1}$ per 100 km).

deep. In the northern lowlands, where the crust is no more than 30 km thick, the BDT is controlled by the mantle rheology and is 60 to 100 km deep. The penetration depth depends on the geotherm, which should be less than 15 $K.km^{-1}$ in the lowlands and more than 7 $K.km^{-1}$ in the uplands to explain the systematic difference of spacing of ridges in the northern lowlands compared to Solis and Lunae Plana if the effective stress exponent is identical in both regions. A similar penetration depth has been determined from kinematic analysis of individual ridges in Lunae Planum [*Tate et al.*, 2002].

[60] The effective stress exponents that can explain the ridge spacing are between -15 to -25. These values may indicate that localization is dictated by processes active during initial failure of rocks, such as cohesion loss upon failure or nonassociated elastic-plastic flow [*Montési and Zuber*, 2002]. It is therefore unlikely that the fault underlying the ridges existed before the horizontal shortening of the lithosphere that is expressed by the ridges. This is in contrast with another area where a localization instability appears to control fault spacing, the Central Indian Ocean [*Montési and Zuber*, 2003b], or with the terrestrial examples of basement uplift [*Rodgers*, 1987], which have been proposed as terrestrial analogue of deeply rooted wrinkle ridges [*Plescia and Golombek*, 1986; *Golombek et al.*, 2001]. Reactivation explains why the planform and orientation of terrestrial basement uplifts is more irregular than that of Martian wrinkle ridges.

[61] Impact craters influence wrinkle ridges on Mars. Some ridges have a curvilinear planform that probably reflects impact craters buried within or underneath the volcanic plain unit [*Plescia*, 1991; *Raitala and Kauhanen*, 1992; *Head et al.*, 2002] and, statistically, wrinkle ridges are located at a shorter distance from impact craters than if random [*Allemand and Thomas*, 1995]. Although the influence of craters has been used to argue that ridges are only shallowly rooted [*Allemand and Thomas*, 1992, 1995; *Mangold et al.*, 1998], we note that a deeply rooted fault would be likely to use the preexisting heterogeneity constituted by an impact structure as it propagates near the surface. The influence of craters on ridge trajectory does not exclude the ridges being deeply rooted.

6.2. Sediment and Ridge Interaction in the Northern Plains

[62] The morphology of the Martian northern plains and outflow channels at their margin has been reported to support the idea that an ocean may have been present in the lowlands during the Hesperian [*Lucchita et al.*, 1986; *Jöns*, 1990; *Baker et al.*, 1991; *Scott et al.*, 1992; *Parker et al.*, 1989, 1993; *Moore et al.*, 1995; *Head et al.*, 1999; *Parker and Currey*, 2001], contemporaneous to ridge formation. However, these observations have alternative interpretations and the proposed ocean is still controversial [*Malin and Edgett*, 1999, 2001; *Edgett and Malin*, 2000; *Baker*, 2001; *Jakosky and Phillips*, 2001; *McGill*, 2001; *Withers and Neumann*, 2001]. The presence of a Hesperian ocean may be further tested by studying the effects of sedimentation on the northern plains topography. The characteristic roughness of the Vastitas Borealis formation [*Kreslavsky and Head*, 2000] is consistent with $\sim$100 m of sediments covering a unit resembling ridged plains such as Lunae Planum [*Head et al.*, 2002; *Kreslavsky and Head*, 2002]. The power spectrum of northern lowland topography for wavelengths in excess of 10 km is consistent with the expected result of sediment transport [*Aharonson et al.*, 2001]. However, these sediments are not necessarily marine; [*Edgett and Malin*, 2000] report on possible sediments in the northern plains using MOC images, but found no obvious submarine landform. It is worth noting that the landforms interpreted in MOC images as evidence for sediments are also visible in the southern hemisphere, in

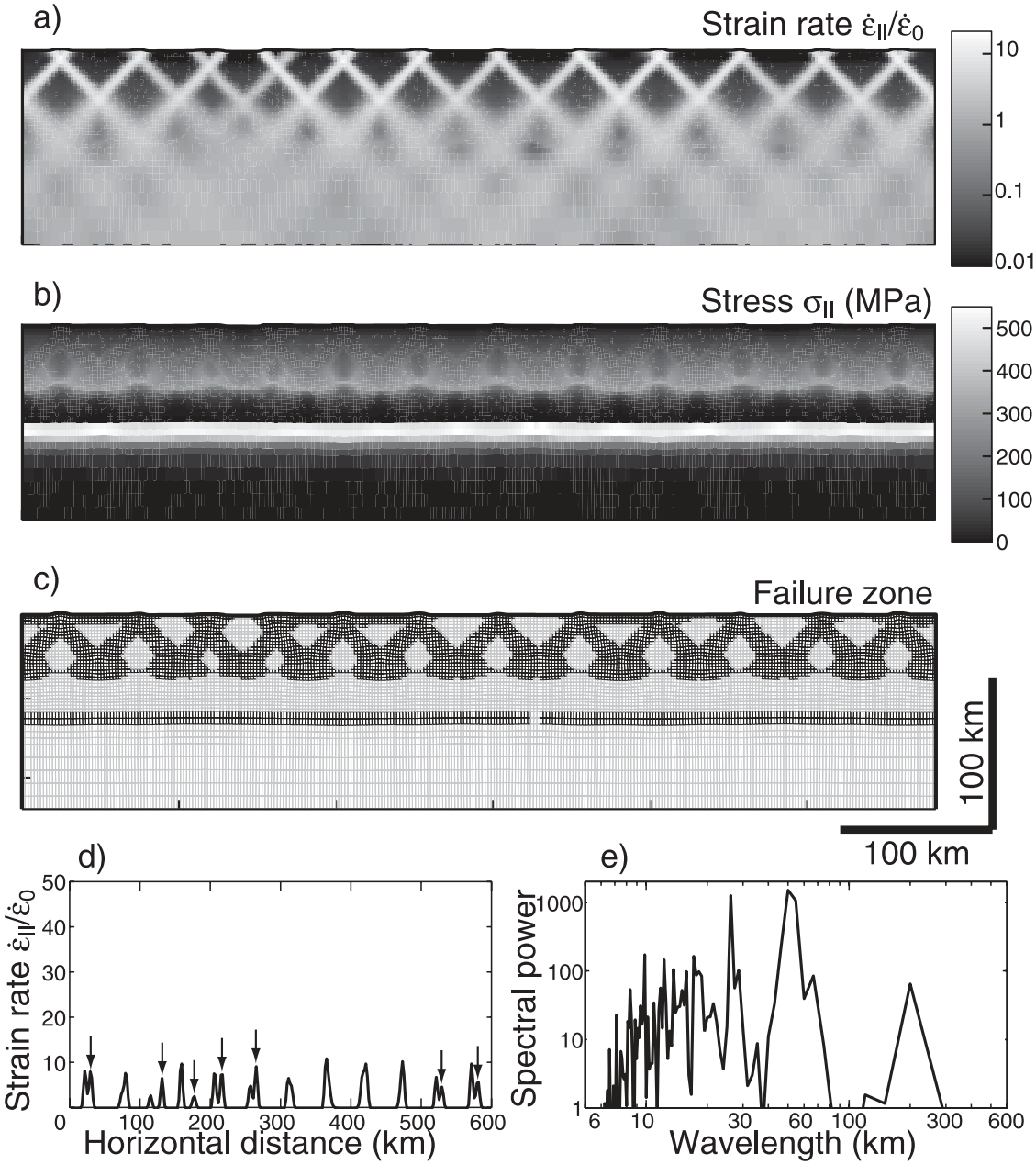

Figure 14. a) Strain rate field, b) stress field, c) failure zone (darker elements), d) surface strain rate, and e) power spectrum of the surface strain rate of the model without crustal thickness or geotherm gradients (Figure 12a) after convergence and localization of the solution. In a), b), and c), a horizontal shortening of 3% was imposed in one time step after deformation field has converged to visualize the deformation field. The vertical arrows in d) indicate left-dipping faults. Strain rate is scaled by $\dot{\varepsilon}_0 = 10^7$ yr^{-1}.

locations where no ocean were proposed [*Malin and Edgett*, 2001]. The topographic roughness of Amazonis Planitia, also in the lowlands but at the limit of the proposed ocean, is compatible with either aeolian or submarine deposition [*Aharonson et al.*, 1998].

[63] The numerous ridges now recognized in the northern lowlands [*Withers and Neumann*, 2001; *Thomson and Head*, 2001; *Head et al.*, 2002] lead to new ways to evaluate sedimentation in that region. *Head et al.* [2002] proposed that the spacing of ridges in the lowlands is a factor of two larger than in the ridged plains because of a sedimentary cover. If the sediments bury completely the smallest ridges, the average spacing of the exposed ridges increases [*Head et al.*, 2002]. However, the ~100 m of sediments required to simulate the roughness characteristics of the Vastitas Borealis formation exceeds the average and median ridge height in nonsedimented plains such as Lunae Planum (Resp. 65 and 47 m [*Head et al.*, 2002]). Most ridges should vanish under such a sediment cover. To increase the ridge spacing by a factor of two, half the ridges must be entirely buried. The level of flooding would then correspond to the median of the distribution of ridge height in ridged plains, 47 m. In

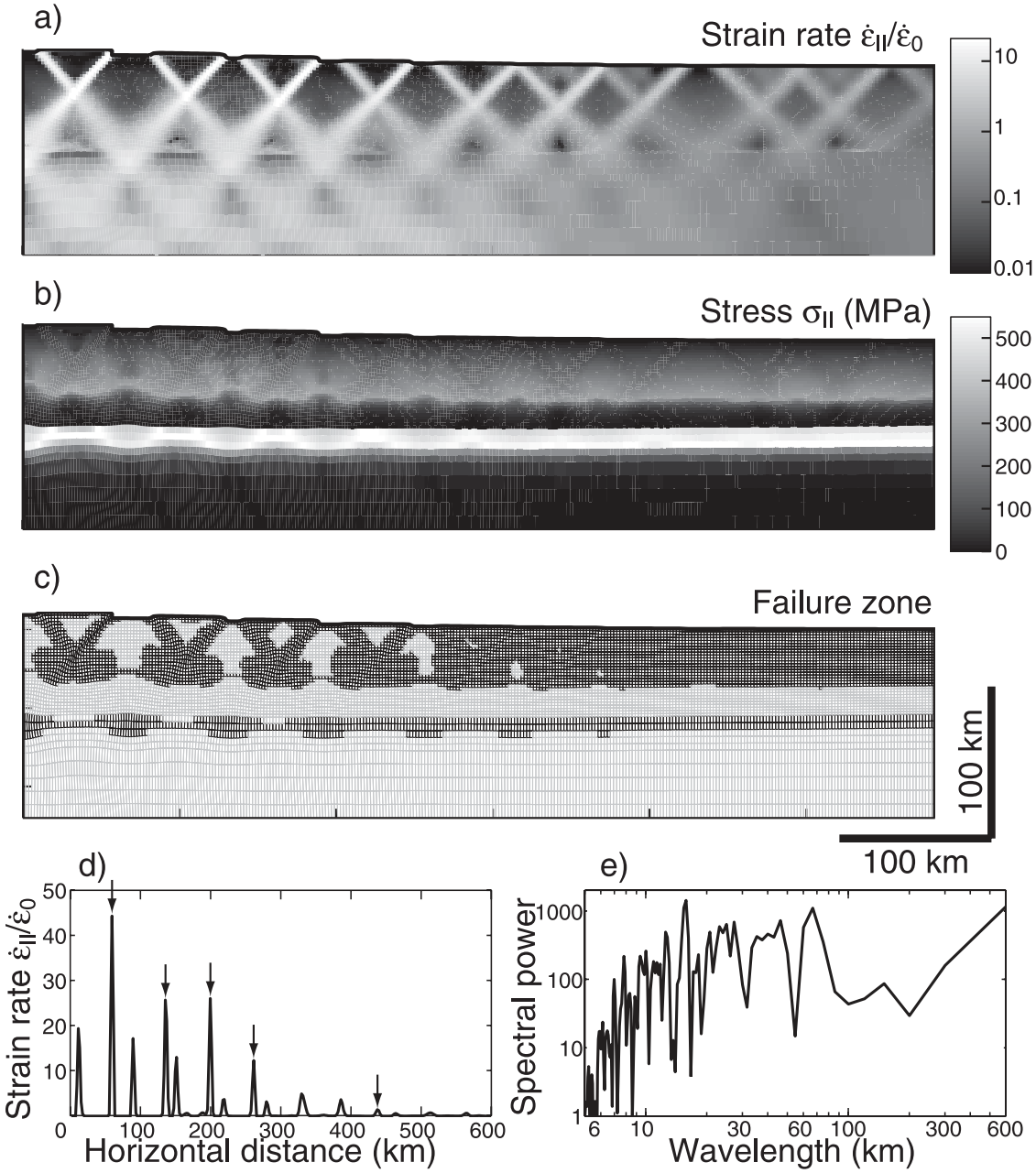

Figure 15. a) Strain rate field, b) stress field, c) failure zone (darker elements), d) surface strain rate, and e) power spectrum of the surface strain rate of the model with a crustal thickness gradient of 1 km per 100 km (Figure 12b) after convergence and localization of the solution. In a), b), and c), a horizontal shortening of 3% was imposed in one time step after deformation field has converged to visualize the deformation field. The vertical arrows in d) indicate left-dipping faults. Strain rate is scaled by $\dot{\varepsilon}_0 = 10^7$ yr^{-1}.

that case, flooding would reduce the maximum-likelihood value of the ridge height distribution by the thickness of the sediments, As the maximum-likelihood value for Lunae Planum ridge heights is also ~50 m [*Head et al.*, 2002], the height distribution of the exposed ridges in the lowlands should decay monotonically or have a small maximum likelihood value, if a sediment flooding model was correct. However, the histograms of exposed ridge height in the lowlands are peaked around 45 to 50 m [*Head et al.*, 2002], similar to the value in the nonsedimented ridged plain. We do not know of a physical mechanism to explain why every other ridge would display a lower amplitude, and therefore be more likely to be buried, than the intervening one, and the bimodal distribution of ridge height expected in that case is not observed in the highland ridges. Hence we conclude that majority of the lowland ridges are still visible: burial of ridges does not explain the factor of two difference in ridge spacing between lowlands and highlands.

[64] Our model shows that the deeper BDT in the lowland than the highlands, due to the thinner crust, can explain the larger ridge spacing in this region. However, the uncertainty in the rheology, heat flux, and strain rate at the time of ridge

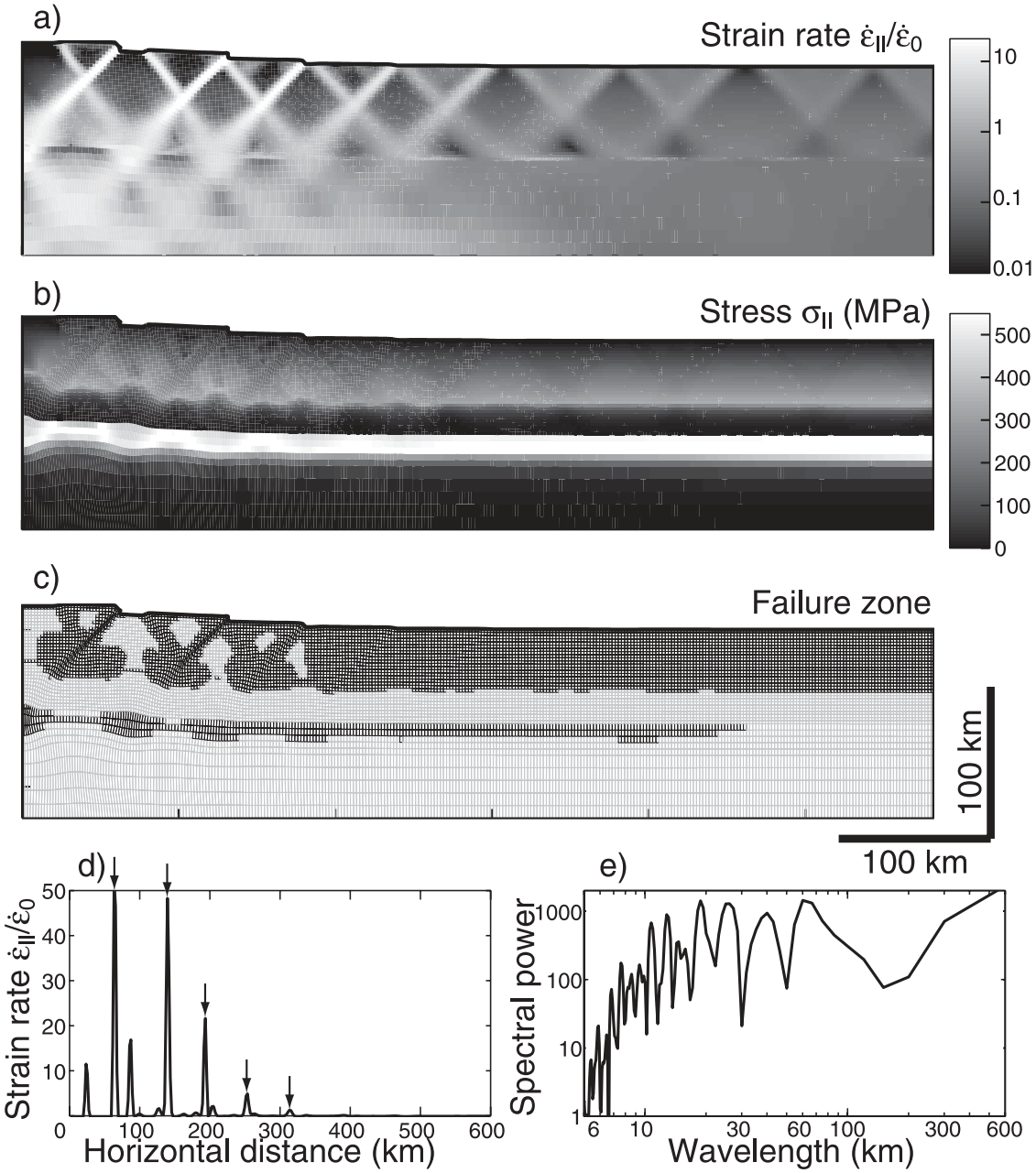

Figure 16. a) Strain rate field, b) stress field, c) failure zone (darker elements), d) surface strain rate, and e) power spectrum of the surface strain rate of the model with a geotherm gradient of 0.2 K.km^{-1} per 100 km (Figure 12a) after convergence and localization of the solution. In a), b), and c), a horizontal shortening of 3% was imposed in one time step after deformation field has converged to visualize the deformation field. The vertical arrows in d) indicate left-dipping faults. Strain rate is scaled by $\dot{\varepsilon}_0 = 10^7$ yr^{-1}.

formation make it impossible to ascertain that the difference in BDT is solely responsible for the large ridge spacing in the lowlands. The morphology of these ridges indicates that they have been degraded and sedimented [*Thomson and Head*, 2001; *Head et al.*, 2002]. Sedimentation effects can certainly modulate the observed ridge spacing, although we doubt that sedimentation alone can explain the difference. *Thomson and Head* [2001] also showed that lowland ridges are longer than highland ridges, which indicates, if the scaling relations between fault length, displacement, and depth are verified at the scale of interest [*Bonnet et al.*, 2001], that the faults underlying lowland ridges penetrate more deeply than those under highland ridges. This is consistent with our explanation of the ridge spacing using a deeper BDT.

[65] We noted that if the northern lowlands are covered by an approximately 100-m thick sediment layer, the majority of the preexisting ridges may be completely buried. Instead, a large fraction of the population is visible. Hence the sediments may be draped over the preexisting ridge-scale topography rather than flooding it. Draped sediments could preserve the ridge topography while smoothing the

smallest length scales. Summit crenulations may be erased in that process, explaining the difficulty in identifying the ridges in visible images. Crater remnants in the northern plains identified in topographic data (stealth craters [*Head et al.*, 2002]) are also more consistent with draping rather than flooding of the topography as they are filled to a level that is systematically below the surrounding plains. *Head et al.* [2002] argue that the entire population of stealth craters is visible in the present topography, with a residual crater depth ~100 m, independent of crater diameter. Therefore the distribution of stealth crater depths indicates that sediment transport has not been able to remove topographic signatures with amplitude ~100 m, the characteristic depth of stealth craters, which is similar to ridge heights. It is therefore possible that most ridges are visible in the current topography.

[66] Sedimentation in the Earth's ocean can be modeled as simultaneous emplacement and downslope-diffusion of sediments over a preexisting topography [*Webb and Jordan*, 1993, 2001a]. Inversion of seafloor bathymetry indicates that the diffusivity of the sediments is ~0.3 ± 0.2 $m^{-2}.yr^{-1}$ for a length scale similar to the ridge spacing [*Webb and Jordan*, 2001b]. Values of diffusivity at least one order of magnitude smaller are required if the sediments are to be draped over the preexisting topography [*Webb and Jordan*, 2001a], as we infer is the case in the Martian lowlands. As scaling by gravity, which is a factor of three smaller on Mars than on the Earth, may not be enough to account for this difference, this might indicate either that the putative ocean was short-lived, which reduces the time during which sediment transport occurs, or that the transporting medium was more viscous than water, as mud is. Both a mud ocean [*Jöns*, 1990; *Tanaka et al.*, 2001] and an episodic short-lived ocean [*Baker et al.*, 1991; *Baker*, 2001; *Kreslavsky and Head*, 2002] have been proposed on the basis of surface morphology, but the evidence is ambiguous.

6.3. Surface Geotherm and Heat Budget of Mars

[67] The thermal evolution of Mars has important implications for the history of volcanism, volatile abundance, and climate [*Weizman et al.*, 2001; *Jakosky and Phillips*, 2001]. The results of thermal models, however, are variable. Some predict intensive melting in present-day Mars [*Schubert et al.*, 1992; *Reese et al.*, 1998], while others, appealing to an early episode of intense cooling [*Nimmo and Stevenson*, 2000; *Choblet and Sotin*, 2001; *Zhong and Zuber*, 2001] or differentiation of heat-producing elements [*Kiefer*, 2001; *Weizman et al.*, 2001], allow the volcanic activity to diminish over time. This is supported by geological observations [*Greeley and Spudis*, 1981].

[68] Constraints on the thermal history of a planet come from estimates of the heat flux. Our modeling of ridge spacing implies a geotherm dT/dz = 12 ± 3 $K.km^{-1}$ in the ridged plains and in the northern lowlands. We cannot resolve differences between the two regions. Hence the corresponding heat flux, $q_s \sim 37 \pm 10$ $mW.m^{-2}$ may be taken as representative of Mars during the time of ridge formation, the Hesperian (3.7 to 3.0 Gyr ago, [*Hartmann and Neukum*, 2001]. Smaller heat flux would be implied if the surface temperature or the strain rate were higher than assumed here.

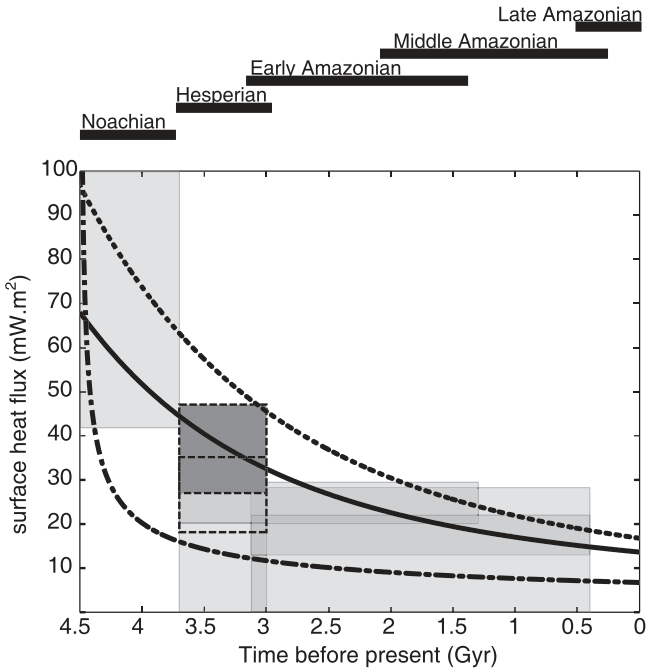

Figure 17. Estimates of Martian surface heat flux. Darkest box: our analysis of ridge spacing; Semi-transparent boxes: admittance analyses from *McGovern et al.* [2002]. Dashed boxes indicate analyses of Hesperian plains. Lines: heat flux needed to balance radiogenic heat production using the chemical models of *Treiman et al.* [1986] (solid line) and *Laul et al.* [1986] (dashes); prediction from lithosphere cooling (dash-dots). The bars above the graph indicate the time span of Martian epochs from *Hartmann and Neukum* [2001].

[69] Heat flux can also be determined from modeling of elastic flexure, constrained by the topography and the gravity field of the planet [*Turcotte and Schubert*, 1982; *Comer et al.*, 1985; *Wieczorek and Phillips*, 1998]. Admittance analyses of Mars Global Surveyor data [*Zuber et al.*, 2000; *McGovern et al.*, 2002; *McKenzie et al.*, 2002; *Nimmo*, 2002] constrain the effective elastic thickness, T_e, for several regions of Mars, which can be converted in a heat flow estimate. The most ancient terrains show very little elastic support ($T_e \sim 0$, $q_s \rightarrow \infty$), whereas the most recent terrains appear almost rigid ($T_e \rightarrow \infty$, $q_s \rightarrow 0$). The thickening of T_e with time is interpreted to reflect cooling of the planet.

[70] The heat flux in the Hesperian-age Solis Planum is constrained from admittance studies to be between 18 and 35 $mW.m^{-2}$ [*McGovern et al.*, 2002], slightly lower than our estimates for the same region (27 to 47 $mW.m^{-2}$). However, the admittance analysis indicates significant subsurface loading [*McGovern et al.*, 2002], the timing of which is not constrained. As our estimate of the Hesperian heat flux fits well into the time evolution of heat flux determined by elastic flexure analysis we consider that the flexural and ridge spacing analyses are broadly consistent (Figure 17).

[71] The gradual decrease of heat flux with time, apparent in Figure 17, has been attributed to cooling of the litho-

sphere [*Zuber et al.*, 2000], as for the heat flux of the Earth's ocean floor [*Sclater et al.*, 1980]. If the lithosphere, initially at a temperature T_m, is cooled such that its surface temperature is fixed at T_s, its heat flux is q_s after a time

$$t = \frac{k^2 (T_m - T_s)^2}{\pi \kappa q_s^2} \tag{9}$$

with $\kappa = 8 \times 10^{-7}$ m^2.s^{-1} the thermal diffusivity, and k = 3.1 W.m^{-1}.K^{-1} the thermal conductivity [*Turcotte and Schubert*, 1982]. If we take $T_m - T_s = 1300 \pm 200$ K, the heat flux $q_s = 37 \pm 10$ mW.m^{-2}, compatible with our observations of wrinkle ridges, is attained after only 90 to 300 Myr. Numerous impact basins, even in the northern lowlands [*Frey et al.*, 2002], as well as Rb-Sr and Lu-Hf isotope systematics in Martian meteorites [*Borg et al.*, 1997; *Blichert-Toft et al.*, 1999] attest that the lithosphere formed in the earliest Martian history. The wrinkle ridges of Solis Planum and the northern lowlands, of middle to late Hesperian age, formed ~1 Gyr after formation of the lithosphere. The heat flux that we infer from the spacing of the ridges is higher than the simple cooling model predicts.

[72] As the heat flux compatible with geological and geophysical observations exceeds that predicted by plate cooling, a contribution of radiogenic heating or secular cooling is required. We compare in Figure 17 the heat flux deduced from flexure and ridge spacing models with the surface heat flux needed to transport the heat produced in the Martian interior according to the composition models of *Treiman et al.* [1986] and *Laul et al.* [1986]. The heat flux inferred from our analysis follows closely the decay trend of the radiogenic heat production. This implies that the heat evacuated at the surface was roughly balanced by the heat produced in the interior. Hence the mantle temperature may have stayed roughly constant with time. If the mantle was cooled early on either by an episode of plate tectonics [*Nimmo*, 2002] or degree-1 convection [*Zhong and Zuber*, 2001], it could have remained at relatively low temperature, and volcanism would be progressively less important, due to the progressive thickening of the lithosphere.

7. Conclusions

[73] With the recent discovery of wrinkle ridges in the Martian northern lowlands [*Withers and Neumann*, 2001; *Head et al.*, 2002], the penetration depth of ridge-related faulting as well as the structure of the lithosphere in the Hesperian can be constrained. The spacing of lowland ridges is a factor of two greater than in other ridged plains, which may reflect a two-fold increase in the depth of the brittle-ductile transition arising from variations of the crustal thickness. In the ridged plains, where the crust is relatively thick, the lower crust may be ductile, in which case faulting is limited by the brittle-ductile transition of crustal rocks. In the lowlands, the thinner crust may be brittle throughout, so that faulting is limited by the brittle-ductile transition of mantle rocks. If we use a combination of diabase [*Caristan*, 1982] and dry olivine [*Karato et al.*, 1986] as controlling the ductile strength of the crust and the mantle, respectively, the factor of two increase is explained. The implied geotherm, tied to the crustal thickness derived from MGS data [*Zuber et al.*, 2000], is 12 ± 3 K.km^{-1}, without any resolvable difference between the two regions. Such a heat flux is comparable with the heat produced by radiogenic decay during the Hesperian.

[74] Penetration of ridge-related strains to the brittle-ductile transition categorized the wrinkle ridges as thick-skinned tectonics, like basement uplifts on Earth [*Rodgers*, 1987]. The recent analogy of wrinkle ridges with folds forced by a blind thrust [*Schultz*, 2000] is also consistent with deep penetration of the faults underlying wrinkle ridges. The ratio of ridge spacing to depth of faulting is ~1, too small to be explained by buckling of the lithosphere. However, the localization instability developed by *Montési and Zuber* [2003a] can explain this ratio. The efficiency of localization, determined from the ridge spacing, points toward failure of intact rock, as opposed to reactivation of a preexisting structure. This inference is however subject to caution, because of the wide ranges of localization efficiency associated with localization mechanisms [*Montési and Zuber*, 2002]. With a lithospheric structure similar to that implied by the ridge spacing analysis, faults dipping toward high-standing areas can be preferentially activated by even minor lateral variations of crustal thickness or geotherm. Such a pattern of faulting is indeed observed in Solis Planum [*Golombek et al.*, 2001].

[75] **Acknowledgments.** We thank Oded Aharonson for assistance with the MOLA data, and Matt Golombek, Jim Head, Misha Kreslavsky, Chris Okubo, Rich Schultz, and Paul Withers for their comments on ridge tectonics and morphology. We benefited from reviews by Roger Phillips and an anonymous reviewer. This work was supported by NASA grant NAG5-4555.

References

Aharonson, O., M. T. Zuber, G. A. Neumann, and J. W. Head III, Mars: Northern hemisphere slopes and slope distribution, *Geophys. Res. Lett.*, *25*, 4413–4416, 1998.

Aharonson, O., M. T. Zuber, and D. H. Rothman, Statistics of Mars's topography from the Mars Orbiter Laser Altimeter: Slopes, correlations, and physical models, *J. Geophys. Res.*, *106*, 23,723–23,735, 2001.

Allemand, P., and P. Thomas, Modèle fragile des rides martiennes contraint par la géométrie de surface, *C. R. Acad. Sci., Ser. II*, *315*, 1397–1402, 1992.

Allemand, P., and P. Thomas, Localization of Martian ridges by impact craters: Mechanical and chronological implications, *J. Geophys. Res.*, *100*, 3251–3262, 1995.

Baker, V. R., Water and the Martian landscape, *Nature*, *412*, 228–236, 2001.

Baker, V. R., R. G. Strom, V. C. Gulick, J. S. Kargel, G. Komatsu, and V. S. Kale, Ancient oceans, ice sheets, and the hydrological cycle on Mars, *Nature*, *352*, 589–594, 1991.

Bandfield, J. L., V. E. Hamilton, and P. R. Christensen, A global view of Martian surface compositions from MGS-TES, *Science*, *287*, 1626–1630, 2000.

Banerdt, W. B., R. J. Phillips, N. H. Sleep, and R. S. Saunders, Thick shell tectonics on one-plate planets: Applications to Mars, *J. Geophys. Res.*, *87*, 9723–9733, 1982.

Banerdt, W. B., M. P. Golombek, and K. L. Tanaka, Stress and tectonics on Mars, in *Mars*, edited by H. H. Kieffer et al., pp. 249–297, Univ. of Ariz. Press, Tucson, 1992.

Banerdt, W. B., G. E. McGill, and M. T. Zuber, Plain tectonics on Venus, in *Venus II*, edited by S. W. Bougher, D. M. Hunten, and R. J. Phillips, pp. 901–930, Univ. of Ariz. Press, 1997.

Bathe, K.-J., *Finite Elements Procedures*, Prentice-Hall, Old Tappan, N. J., 1996.

Behn, M. D., J. Lin, and M. T. Zuber, A continuum mechanics model for normal faulting using a strain-rate softening rheology: Implications for thermal and rheological controls on continental and oceanic rifting, *Earth Planet. Sci. Lett.*, *202*, 725–740, 2002.

Bilotti, F., and J. Suppe, The global distribution of wrinkle riges of Venus, *Icarus*, *139*, 137–139, 1999.

Biot, M. A., Theory of folding of stratified viscoelastic media and its implications in tectonics and orogenesis, *Geol. Soc. Am. Bull.*, *72*, 1595–1620, 1961.

Blichert-Toft, J., J. D. Gleason, P. Télouk, and F. Albarède, The Lu-Hf isotope geochemistry of shergottites and the evolution of the Martian mantle-crust system, *Earth Planet. Sci. Lett.*, *173*, 25–39, 1999.

Bonnet, E., O. Bour, N. E. Odling, P. Davy, I. Main, P. Cowie, and B. Berlowitz, Scaling of fracture systems in geological media, *Rev. Geophys.*, *39*, 347–383, 2001.

Borg, L. E., L. E. Nyquist, L. A. Taylor, H. Weismann, and C.-Y. Shih, Constraints on Martian differentiation processes from Rb-Sr and Sm-Nd isotopic analyses of the basaltic shergottite QUE 94201, *Geochim. Cosmochim. Acta*, *61*, 4915–4931, 1997.

Byerlee, J. D., Friction of rocks, *Pure Appl. Geophys.*, *116*, 615–626, 1978.

Caristan, Y., The transition from high temperature creep to fracture in Maryland diabase, *J. Geophys. Res.*, *87*, 6781–6790, 1982.

Carr, M. H., Retention of an atmosphere on early Mars, *J. Geophys. Res.*, *104*, 21,897–21,909, 1999.

Caruso, P., and R. A. Schultz, Slope stability and lithology for interior layered deposits and wallrock in Valles Marineris (abstract), *Lunar Planet. Sci.*, *XXXII*, 1745, 2001.

Chapple, W. M., Mechanics of thin-skinned fold-and-thrust belts, *Geol. Soc. Am. Bull.*, *89*, 1189–1198, 1978.

Chen, Y., and W. J. Morgan, A nonlinear rheology model for mid-ocean ridge axis topography, *J. Geophys. Res.*, *95*, 17,583–17,604, 1990.

Chicarro, A. F., P. H. Schultz, and P. Masson, Global and regional ridge patterns on Mars, *Icarus*, *63*, 153–174, 1985.

Choblet, G., and C. Sotin, Early transient cooling of Mars, *Geophys. Res. Lett.*, *28*, 3035–3038, 2001.

Comer, R. P., S. C. Solomon, and J. W. Head III, Mars: Thickness of the lithosphere from the tectonic response to volcanic loads, *Rev. Geophys.*, *21*, 61–92, 1985.

Dieterich, J. H., Modeling of rock friction: 1. Experimental results and constitutive equations, *J. Geophys. Res.*, *84*, 2161–2168, 1979.

Edgett, K. S., and M. C. Malin, MGS MOC view of the Martian Northern Plains (abstract), *Lunar Planet. Sci.*, *XXXI*, 1054, 2000.

Evans, B., and D. L. Kohlstedt, Rheology of rocks, in *Rock Physics and Phase Relations: A Handbook of Physical Constants*, *AGU Ref. Shelf*, vol. 3, edited by T. J. Ahrens, pp. 148–165, AGU, Washington, D. C., 1995.

Fletcher, R. C., Wavelength selection in the folding of a single layer with power-law rheology, *Am. J. Sci.*, *274*, 1029–1043, 1974.

Fletcher, R. C., and B. Hallet, Unstable extension of the lithosphere: A mechanical model for Basin-and-Range structure, *J. Geophys. Res.*, *88*, 7457–7466, 1983.

Frey, H. V., J. H. Roark, K. M. Shockey, E. L. Frey, and S. E. H. Sakimoto, Ancient lowlands on Mars, *Geophys. Res. Lett.*, *29*(10), 1384, doi:10.1029/2001GL013832, 2002.

Gleason, G. C., and J. Tullis, A flow law for dislocation creep of quartz aggregates determined with the molten salt cell, *Tectonophysics*, *247*, 1–23, 1995.

Golombek, M. P., J. B. Plescia, and B. J. Franklin, Faulting and folding in the formation of planetary wrinkle ridges, *Proc. Lunar Planet. Sci. Conf. 21st*, 679–693, 1991.

Golombek, M. P., F. S. Anderson, and M. T. Zuber, Martian wrinkle ridge topography: Evidence for subsurface faults from MOLA, *J. Geophys. Res.*, *106*, 23,811–23,922, 2001.

Gordon, R. G., Diffuse oceanic plate boundaries: Strain rates, vertically averaged rheology, and comparisons with narrow plate boundaries and stable interiors, in *The History and Dynamics of Global Plate Motions*, edited by M. A. Richards, R. G. Gordon, and R. D. van der Hilst, *Geophys. Monogr. Ser.*, vol. 121, pp. 143–159, AGU, Washington, D. C., 2000.

Goudy, C. L., and T. K. P. Gregg, Insight to the evolution of wrinkle ridges in Hesperia Planum, Mars (abstract), *Lunar Planet. Sci.*, *XXXIII*, 1135, 2002.

Greeley, R., and P. D. Spudis, Volcanism on Mars, *Rev. Geophys.*, *19*, 13–41, 1981.

Hartmann, W. K., and G. Neukum, Cratering chronology and the evolution of Mars, *Space Sci. Rev.*, *96*, 165–194, 2001.

Hauck, S. A., II, and R. J. Phillips, Thermal and crustal evolution of Mars, *J. Geophys. Res.*, *107*(E7), 5052, doi:10.1029/2001JE001801, 2002.

Head, J. W., III, H. Hiesinger, M. A. Ivanov, M. A. Kreslavsky, S. Pratt, and B. Thomson, Possible ancient oceans on Mars: Evidence from Mars Orbiter Laser Altimeter Data, *Science*, *286*, 2134–2137, 1999.

Head, J. W., III, M. A. Kreslavsky, and S. Pratt, Northern lowlands of Mars: Evidence for widespread volcanic flooding and tectonic deformation in the Hesperian period, *J. Geophys. Res.*, *107*(E1), 5003, doi:10.1029/2000JE001445, 2002.

Hirth, G., and D. L. Kohlstedt, Water in the oceanic upper mantle: Implications for rheology, melt extraction and the evolution of the lithosphere, *Earth Planet. Sci. Lett.*, *144*, 93–108, 1996.

Hynek, B., and R. J. Phillips, Evidence for extensive denudation of the Martian highlands, *Geology*, *29*, 407–410, 2001.

Jakosky, B. M., and R. J. Phillips, Mars' volatile and climate history, *Nature*, *412*, 237–244, 2001.

Johnson, A. M., and R. C. Fletcher, *Folding of Viscous Layers*, Cambridge Univ. Press, New York, 1994.

Jöns, H. P., Das Relief des Mars: Versuch einer zusammenfassenden übersicht, Teil III, *Geol. Rundsch.*, *79*, 131–164, 1990.

Karato, S.-I., M. Paterson, and J. Fitz Gerald, Rheology of synthetic olivine aggregates: Influence of grain size and water, *J. Geophys. Res.*, *91*, 8151–8176, 1986.

Kiefer, W. S., Mantle convection on Mars with enhanced crustal radioactivity: Implications for geophysical and geological observables (abstract), *Lunar Planet. Sci.*, *XXXII*, 1949, 2001.

Korenaga, J., and P. B. Kelemen, Major element heterogeneity in the mantle source of the north atlantic igneous province, *Earth Planet. Sci. Lett.*, *184*, 251–268, 2000.

Kreslavsky, M. A., and J. W. Head III, Kilometer-scale roughness of Mars: Results from MOLA data analysis, *J. Geophys. Res.*, *105*, 15,051–15,059, 2000.

Kreslavsky, M. A., and J. W. Head III, Fate of outflow channel effluents in the northern lowlands of Mars: The Vastitas Borealis Formation as a sublimation residue from frozen ponded bodies of water, *J. Geophys. Res.*, *107*(E12), 5121, doi:10.1029/2001JE001831, 2002.

Laul, J. C., et al., Chemical systematics of the shergotty meteorite and the composition of its parent body (Mars), *Geochim. Cosmochim. Acta*, *50*, 909–926, 1986.

Longhi, J., E. Knittle, J. R. Holloway, and H. Wänke, The bulk composition, mineralogy and internal structure of Mars, in *Mars*, edited by H. H. Kieffer et al., pp. 184–208, Univ. of Ariz. Press, Tucson, 1992.

Lucchita, B. K., and J. L. Klockenbrink, Ridges and scarps in equatorial belts of Mars, *Moon Planets*, *24*, 415–429, 1981.

Lucchita, B. K., H. M. Ferguson, and C. Summers, Sedimentary deposits in the Northern lowland plains, Mars, *Proc. Lunar Planet. Sci. Conf. 17th*, Part 1, *J. Geophys. Res.*, *91*, suppl., E166–E174, 1986.

Malin, M. C., and K. S. Edgett, Oceans or seas in the Martian northern lowlands: High resolution imaging tests of proposed coastlines, *Geophys. Res. Lett.*, *26*, 3049–3052, 1999.

Malin, M. C., and K. S. Edgett, Mars Global Surveyor Mars Orbiter Camera: Interplanetary cruise through primary mission, *J. Geophys. Res.*, *106*, 23,429–23,570, 2001.

Mangold, N., P. Allemand, and P. G. Thomas, Wrinkle ridges of Mars: Structural analysis and evidence for shallow deformation by ice-rich décollements, *Planet. Space Sci.*, *46*, 345–356, 1998.

Mangold, N., P. Allemand, P. G. Thomas, and G. Vidal, Chronology of compressional deformation on Mars: Evidence for a single and global origin, *Planet. Space Sci.*, *48*, 1201–1211, 2000.

Martinod, J., and P. Davy, Periodic instabilities during compression or extension of the lithosphere: 2. Analogue experiments, *J. Geophys. Res.*, *99*, 12,057–12,069, 1994.

Maxwell, T. A., Orientation and origin of ridges in the Lunae Palus-Coprates region of Mars, *Proc. Lunar Planet. Sci. Conf. 13th*, Part 1, *J. Geophys. Res.*, *87*, suppl., A97–A108, 1982.

McEwen, A. S., M. C. Malin, M. H. Carr, and W. K. Hartmann, Voluminous volcanism on early Mars revealed in Valles Marineris, *Nature*, *397*, 584–586, 1999.

McGill, G. E., The Utopia basin revisited: Regional slope and shorelines from MOLA profiles, *Geophys. Res. Lett.*, *28*, 411–414, 2001.

McGovern, P. J., S. C. Solomon, D. E. Smith, M. T. Zuber, M. Simons, M. A. Wieczorek, R. J. Phillips, G. A. Neumann, O. Aharonson, and J. W. Head, Localized gravity/topography admittance and correlation spectra on Mars: Implications for regional and global evolution, *J. Geophys. Res.*, *107*(E12), 5136, doi:10.1029/2002JE001854, 2002.

McKenzie, D., D. N. Barnett, and D.-N. Yuan, The relationship between Martian gravity and topography, *Earth Planet. Sci. Lett.*, *195*, 1–16, 2002.

McSween, H. Y., Jr., What have we learned about Mars from SNC meteorites?, *Meteoritics*, *29*, 757–779, 1994.

McSween, H. Y., Jr., et al., Chemical, multispectral, and textural constraints on the composition and origin of rocks at the Mars Pathfinder site, *J. Geophys. Res.*, *104*, 8679–8715, 1999.

Montési, L. G. J., Localization instability and the origin of regularly-spaced faults in planetary lithospheres, Ph.D., Mass. Inst. of Technol., Cambridge, 2002.

Montési, L. G. J., and M. T. Zuber, A unified description of localization for application to large-scale tectonics, *J. Geophys. Res.*, *107*(B3), 2045, doi:10.1029/2001JB000465, 2002.

Montési, L. G. J., and M. T. Zuber, Spacing of faults at the scale of the lithosphere and localization instability: 1. Theory, *J. Geophys. Res.*, *108*(B2), 2110, doi:10.1029/2002JB001923, 2003a.

Montési, L. G. J., and M. T. Zuber, Spacing of faults at the scale of the lithosphere and localization instability: 2. Application to the Central Indian Basin, *J. Geophys. Res.*, *108*(B2), 2111, doi:10.1029/2002JB001924, 2003b.

Moore, J. M., G. D. Clow, W. L. Davis, V. C. Gulick, D. R. Janke, C. P. McKay, C. R. Stoker, and A. P. Zent, The circum-Chryse region as a possible example of a hydrologic cycle on Mars: Geologic observations and theoretical evaluation, *J. Geophys. Res.*, *100*, 5433–5447, 1995.

Neumann, G. A., and M. T. Zuber, A continuum approach to the developement of normal faults, in *Proceedings of the 25th US Symposium on Rock Mechanics*, edited by J. J. K. Daemen and R. A. Schultz, pp. 191–198, A. A. Balkema, Brookfield, Vt., 1995.

Nimmo, F., Admittance estimates of mean crustal thickness and density at the Martian hemispheric dichotomy, *J. Geophys. Res.*, *107*(E11), 5117, doi:10.1029/2002JE001488, 2002.

Nimmo, F., and D. J. Stevenson, Influence of early plate tectonics on the thermal evolution and magnetic field of Mars, *J. Geophys. Res.*, *105*, 11,969–11,980, 2000.

Nimmo, F., and D. J. Stevenson, Estimates of Martian crustal thickness from viscous relaxation of topography, *J. Geophys. Res.*, *106*, 5085–5097, 2001.

Niño, F., H. Philip, and J. Chéry, The role of bed-parallel slip in the formation of blind thrust faults, *J. Struct. Geol.*, *20*, 503–516, 1998.

Noble, S. K., and C. M. Pieters, Type 2 terrain: Compositional constraints on the Martian lowlands (abstract), *Lunar Planet. Sci.*, *XXXII*, 1230, 2001.

Norman, M. D., The composition and thickness of the Martian crust estimated from rare Earth elements and Neodynium isotopic compositions of Martian meteorites, *Meteorit. Planet. Sci.*, *34*, 439–449, 1999.

Norman, M. D., Thickness and composition of the Martian crust revisited: Implications of an ultradepleted mantle with a Nd isotopic composition like that of QUE94201 (abstract), *Lunar Planet. Sci.*, *XXXIII*, 1175, 2002.

Okubo, C. H., and R. A. Schultz, Elevation offsets across wrinkle ridges: Key to structural width (abstract), *Lunar Planet. Sci.*, *XXXII*, 2086, 2001.

Okubo, C. H., and R. A. Schultz, Fault geometry below wrinkle ridges based on slope asymmetry and implications for mechanical stratigraphy (abstract), *Lunar Planet. Sci.*, *XXXIII*, 1708, 2002.

Parker, T. J., and C. R. Currey, Extraterrestrial coastal geomorphology, *Geomorphology*, *37*, 303–328, 2001.

Parker, T. J., R. S. Saunders, and D. M. Schneeberger, Transitional morphology in West Deuteronilus Mensae, Mars: Implications for modification of the lowland/upland boundary, *Icarus*, *82*, 111–145, 1989.

Parker, T. J., D. S. Gorsline, R. S. Saunders, D. C. Pieri, and D. M. Schneeberger, Coastal morphology of the Martian northern plains, *J. Geophys. Res.*, *98*, 11,061–11,078, 1993.

Peulvast, J.-P., D. Mège, J. Chiciak, F. Costard, and P. L. Masson, Morphology, evolution, and tectonics of Valles Marineris wallslopes (Mars), *Geomorphology*, *37*, 329–352, 2001.

Plescia, J. B., Wrinkle ridges in Lunae Planum Mars: Implications for shortening and strain, *Geophys. Res. Lett.*, *18*, 913–916, 1991.

Plescia, J. B., and M. P. Golombek, Origin of planetary wrinkle ridges based on the study of terrestrial analogs, *Geol. Soc. Am. Bull.*, *97*, 1289–1299, 1986.

Raitala, J., Superposed ridges of the Hesperia Planum area on Mars, *Earth Moon Planets*, *40*, 71–99, 1988.

Raitala, J., and K. Kauhanen, Ridge systems related to Martian impact craters, *Earth Moon Planets*, *58*, 65–78, 1992.

Reese, C. C., V. S. Solomatov, and L.-N. Moresi, Heat transport efficiency for stagnant lid convection with dislocation viscosity: Application to Mars and Venus, *J. Geophys. Res.*, *103*, 13,643–16,457, 1998.

Ricard, Y., and C. Froidevaux, Stretching instabilities and lithospheric boudinage, *J. Geophys. Res.*, *91*, 8314–8324, 1986.

Rodgers, J., Chains of basement uplifts within cratons marginal to orogenic belts, *Am. J. Sci.*, *287*, 661–692, 1987.

Ruina, A. L., Slip instability and state-variable friction laws, *J. Geophys. Res.*, *88*, 10,359–10,370, 1983.

Saunders, R. S., T. G. Bills, and L. Johansen, The ridged plains on Mars (abstract), *Lunar Planet. Sci.*, *XII*, 924–925, 1981.

Schubert, G., S. C. Solomon, D. L. Turcotte, M. J. Drake, and N. H. Sleep, Origin and thermal evolution of Mars, in *Mars*, edited by H. H. Kieffer et al., pp. 147–183, Univ. of Ariz. Press, Tucson, 1992.

Schultz, R. A., Localization of bedding-plane slip and backthrust faults above blind thrust faults: Keys to wrinkle ridge structure, *J. Geophys. Res.*, *105*, 12,035–12,052, 2000.

Sclater, J. G., C. Jaupart, and D. Galson, The heat flow through oceanic and continental crust and the heat loss of the Earth, *Rev. Geophys.*, *18*, 269–312, 1980.

Scott, D. H., M. G. Chapman, J. W. Rice, and J. M. Dohm, New evidence of lacustrine basins on Mars: Amazonis and Utopia Planitiae, *Proc. Lunar Planet. Sci. Conf. 22nd*, 53–62, 1992.

Shen, Y., S. C. Solomon, I. T. Bjarnason, and C. J. Wolfe, Seismic evidence for a lower mantle origin of the Iceland mantle plume, *Nature*, *395*, 62–65, 1998.

Sleep, N. H., Martian plate tectonics, *J. Geophys. Res.*, *99*, 5639–5655, 1994.

Smith, D. E., and M. T. Zuber, The crustal thickness of Mars: Accuracy and resolution (abstract), *Lunar Planet. Sci.*, *XXXIII*, 1893, 2002.

Smith, D. E., et al., The global topography of Mars and implications for surface evolution, *Science*, *284*, 1495–1503, 1999.

Smith, D. E., et al., Mars Orbiter Laser Altimeter (MOLA): Experiment summary after the year of global mapping of Mars, *J. Geophys. Res.*, *106*, 23,689–23,723, 2001.

Smith, R. B., Formation of folds, boudinage, and mullions in non-Newtonian materials, *Geol. Soc. Am. Bull.*, *88*, 312–320, 1977.

Smith, R. B., The folding of a strongly non-Newtonian layer, *Am. J. Sci.*, *279*, 272–287, 1979.

Sohl, F., and T. Spohn, The interior structure of Mars: Implications from SNC meteorites, *J. Geophys. Res.*, *102*, 1613–1635, 1997.

Tanaka, K. L., W. B. Banerdt, J. S. Kargel, and N. Hoffman, Huge CO_2-charged debris-flow deposits and tectonics sagging in the northern plains of Mars, *Geology*, *29*, 427–430, 2001.

Tate, A., K. J. Mueller, and M. P. Golombek, Geometry and kinematics of wrinkle ridges on Lunae and Solis Plana, Mars: Implications for fault/fold growth history (abstract), *Lunar Planet. Sci.*, *XXXIII*, 1836, 2002.

Thomson, B. J., and J. W. Head III, Utopia Basin, Mars: Characterization of topography and morphology and assessment of the origin and evolution of basin internal structure, *J. Geophys. Res.*, *106*, 23,209–23,230, 2001.

Tracadas, P. W., and M. T. Zuber, What a global stress map of Venus reveals (abstract), *Lunar Planet. Sci.*, *XXXI*, 1895, 1998.

Treiman, A. H., M. J. Drake, N.-J. Janssens, R. Wolf, and M. Enihara, Core formation in the Earth and shergottite parent body, *Geochim. Cosmochim. Acta*, *50*, 1061–1070, 1986.

Tsenn, M. C., and N. L. Carter, Upper limits of power law creep of rocks, *Tectonophysics*, *136*, 1–26, 1987.

Turcotte, D. L., and G. Schubert, *Geodynamics: Applications of Continuum Physics to Geological Problems*, John Wiley, New York, 1982.

Watters, T. R., Wrinkle ridge assemblages on the terrestrial planets, *J. Geophys. Res.*, *93*, 10,236–10,254, 1988.

Watters, T. R., Origin of periodically spaced wrinkle ridges on the Tharsis plateau of Mars, *J. Geophys. Res.*, *96*, 15,599–15,616, 1991.

Watters, T. R., System of tectonic features common to Earth, Mars, and Venus, *Geology*, *20*, 609–612, 1992.

Watters, T. R., Compressional tectonism on Mars, *J. Geophys. Res.*, *98*, 17,049–17,060, 1993.

Watters, T. R., and T. A. Maxwell, Orientation, relative age, and extent of the Tharsis plateau ridge system, *J. Geophys. Res.*, *91*, 8113–8125, 1986.

Watters, T. R., and M. S. Robinson, Radar and photoclinometric studies of wrinkle ridges on Mars, *J. Geophys. Res.*, *102*, 10,889–10,903, 1997.

Webb, H. F., and T. H. Jordan, Quantifying the distribution and transport of pelagic sediments on young abyssal hills, *Geophys. Res. Lett.*, *20*, 2203–2206, 1993.

Webb, H. F., and T. H. Jordan, Pelagic sedimentation on rough seafloor topography: 1. Forward model, *J. Geophys. Res.*, *106*, 30,433–30,449, 2001a.

Webb, H. F., and T. H. Jordan, Pelagic sedimentation on rough seafloor topography: 2. Inversion results from the North Atlantic Acoustic Reverberation Corridor, *J. Geophys. Res.*, *106*, 30,451–30,473, 2001b.

Weizman, A., D. J. Stevenson, D. Prialnik, and M. Podolak, Modeling the volcanism on Mars, *Icarus*, *150*, 195–205, 2001.

Wieczorek, M. A., and R. J. Phillips, Potential anomalies on a sphere: Applications to the thickness of the lunar crust, *J. Geophys. Res.*, *103*, 1715–1724, 1998.

Wieczorek, M. A., and M. T. Zuber, The thickness of the Mars crust as inferred from geoid-to-topography ratios (abstract), *Lunar Planet. Sci.*, *XXXIII*, 1390, 2002.

Withers, P., and G. A. Neumann, Enigmatic northern plains of Mars, *Nature*, *410*, 652, 2001.

Wyatt, M. B., and H. Y. McSween Jr., Spectral evidence for weathered basalt as an alternative to andesite in the northern lowlands of Mars, *Nature*, *417*, 263–266, 2002.

Zhong, S., and M. T. Zuber, Degree-1 mantle convection and the crustal dichotomy on Mars, *Earth Planet. Sci. Lett.*, *189*, 75–84, 2001.

Zuber, M. T., Compression of oceanic lithosphere: An analysis of intraplate deformation in the Central Indian Basin, *J. Geophys. Res.*, *92*, 4817–4825, 1987.

Zuber, M. T., Wrinkle ridges, reverse faulting, and the depth of penetration of lithospheric strain in Lunae Planum, Mars, *Icarus*, *114*, 80–92, 1995.

Zuber, M. T., The crust and mantle of Mars, *Nature*, *412*, 220–227, 2001.

Zuber, M. T., and L. L. Aist, The shallow structure of the Martian lithosphere in the vicinity of the ridged plains, *J. Geophys. Res.*, *95*, 14,125–14,230, 1990.

Zuber, M. T., and E. M. Parmentier, Finite amplitude folding of a continuously viscosity-stratified lithosphere, *J. Geophys. Res.*, *101*, 5489–5498, 1996.

Zuber, M. T., et al., Internal structure and early thermal evolution of Mars from Mars Global Surveyor topography and gravity, *Science*, *287*, 1788–1793, 2000.

L. G. J. Montési, Department of Geology and Geophysics, Woods Hole Oceanographic Institution, MS 22, Woods Hole, MA 02543, USA. (montesi@whoi.edu)

M. T. Zuber, Department of Earth, Atmospheric, and Planetary Sciences, Massachusetts Institute of Technology, Cambridge, MA 02139, USA. (zuber@mit.edu)